Bright polar mesospheric clouds formed by main engine exhaust from the space shuttle's final launch

Michael H. Stevens,[1] Stefan Lossow,[2,3] Jens Fiedler,[4] Gerd Baumgarten,[4] Franz-Josef Lübken,[4] Kristofer Hallgren,[5,6] Paul Hartogh,[5] Cora E. Randall,[7] Jerry Lumpe,[8] Scott M. Bailey,[9] R. Niciejewski,[10] R. R. Meier,[11] John M. C. Plane,[12] Andrew J. Kochenash,[13] Donal P. Murtagh,[14] and Christoph R. Englert[1]

[1] The space shuttle launched for the last time on 8 July 2011. As with most shuttle launches, the three main engines injected about 350 t of water vapor between 100 and 115 km off the east coast of the United States during its ascent to orbit. We follow the motion of this exhaust with a variety of satellite and ground-based data sets and find that (1) the shuttle water vapor plume spread out horizontally in all directions over a distance of 3000 to 4000 km in 18 h, (2) a portion of the plume reached northern Europe in 21 h to form polar mesospheric clouds (PMCs) that are brighter than over 99% of all PMCs observed in that region, and (3) the observed altitude dependence of the particle size is reversed with larger particles above smaller particles. We use a one-dimensional cloud formation model initialized with predictions of a plume diffusion model to simulate the unusually bright PMCs. We find that eddy mixing can move the plume water vapor down to the mesopause near 90 km where ice particles can form. If the eddy diffusion coefficient is 400 to 1000 m^2/s, the predicted integrated cloud brightness is in agreement with both satellite and ground-based observations of the shuttle PMCs. The propellant mass of the shuttle is about 20% of that from all vehicles launched during the northern 2011 PMC season. We suggest that the brightest PMC population near 70°N is formed by space traffic exhaust.

Citation: Stevens, M. H., et al. (2012), Bright polar mesospheric clouds formed by main engine exhaust from the space shuttle's final launch, *J. Geophys. Res.*, *117*, D19206, doi:10.1029/2012JD017638.

1. Introduction

[2] During each space shuttle launch about 350 tons of water vapor exhaust from the three main engines are injected between 100 and 115 km in a trail about 1000 km long off the east coast of the United States. Since the first reported observation of shuttle main engine exhaust in the upper atmosphere ten years ago, many have studied the diffusion, transport and ultimate fate of these concentrated water vapor plumes. Several showed that its meridional transport can be much faster than either general circulation models or satellite wind climatologies predict [*Stevens et al.*, 2002; *Siskind et al.*, 2003; *Niciejewski et al.*, 2011; *Pumphrey et al.*, 2011; *Meier et al.*, 2011]. Others showed that this transport can be global in scale, leading to remarkable bursts of polar mesospheric clouds (PMCs) in the summertime [*Stevens et al.*, 2003; *Collins et al.*, 2009; *Kelley et al.*, 2010] that can constitute 10 to 20% of the PMC ice mass in either an Arctic or Antarctic summer [*Stevens et al.*, 2005a, 2005b]. This is important because PMCs have been implicated as indicators of climate change [e.g., *Thomas*, 1996] and reported PMC trends are on the order of 1% per year or less [*DeLand et al.*, 2007; *Shettle et al.*, 2009].

[1]Space Science Division, Naval Research Laboratory, Washington, D.C., USA.

[2]Institute of Meteorology and Climate Research, Karlsruhe Institute of Technology, Leopoldshafen, Germany.

[3]Also at Department of Earth and Space Sciences, Chalmers University of Technology, Göteburg, Sweden.

[4]Institute for Atmospheric Physics, Kühlungsborn, Germany.

[5]Max Planck Institute for Solar System Research, Katlenburg-Lindau, Germany.

[6]Also at Institute for Atmospheric Physics, Kühlungsborn, Germany.

[7]Laboratory for Atmospheric and Space Physics and Department of Atmospheric and Oceanic Sciences, University of Colorado at Boulder, Boulder, Colorado, USA.

[8]Computational Physics, Inc., Boulder, Colorado, USA.

[9]Bradley Department of Electrical and Computer Engineering, Virginia Polytechnic and State University, Blacksburg, Virginia, USA.

[10]Space Physics Research Laboratory, University of Michigan, Ann Arbor, Michigan, USA.

[11]School of Physics, Astronomy and Computational Sciences, George Mason University, Fairfax, Virginia, USA.

[12]School of Chemistry, University of Leeds, Leeds, UK.

[13]Computational Physics, Inc., Springfield, Virginia, USA.

[14]Department of Earth and Space Sciences, Chalmers University of Technology, Gothenburg, Sweden.

Corresponding author: M. H. Stevens, Space Science Division, Naval Research Laboratory, Code 7641, 4555 Overlook Ave., SW, Washington, D. C. 20375, USA. (michael.stevens@nrl.navy.mil)
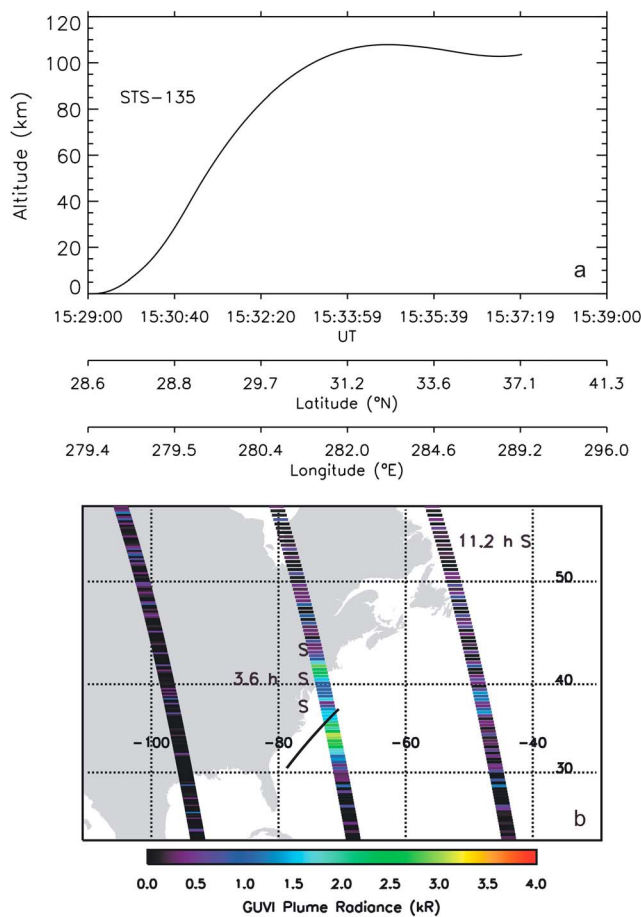
Figure 1. (a) The STS-135 ascent profile on 8 July 2011. Over 300 t of water vapor were injected between 100 and 110 km from the three main engines. (b) Three consecutive orbits of GUVI Lyman-α data, with the middle orbit showing elevated radiances near the ground track of the shuttle plume (in black). The GUVI plume detection was 4.6 h after launch. Locations of four separate SABER limb scans of the water vapor plume obtained 3.6 h after launch (3 scans) and 11.2 h after launch (1 scan) are indicated by an "S." GUVI plume brightnesses are derived from the H Lyman-α channel between 1193 and 1236 Å and are referenced to the color bar. The projected GUVI field-of-view subtends an exaggerated distance for clarity.

[3] Interpretation of the shuttle plume observations challenges our understanding of global scale dynamics and cloud microphysics. The fast meridional transport can in principle be explained by the coupling of tides with the two-day planetary wave [*Liu*, 2007; *Yue and Liu*, 2010], although amplitudes for both tides and planetary waves are currently under-predicted in general circulation models. Recent satellite wind observations suggest that the two-day planetary wave was crucial to the transport of the STS-107 plume to Antarctica in January, 2003 [*Niciejewski et al.*, 2011].

[4] The observed horizontal spreading of the main engine plume is currently not well understood. Although *Kelley et al.* [2009] suggested that the diffusion of photodissociated atomic hydrogen within the plume was anomalously fast, *Meier et al.* [2010, 2011] used a two-dimensional plume

diffusion model to show that classical molecular diffusion can explain the observed plume dimensions for the first 10 h following launch since the hydrogen diffuses upward where it can more rapidly diffuse outward.

[5] Here we present satellite and ground-based observations of the space shuttle main engine plume from its final launch in July 2011. This plume was observed by a variety of instruments capable of measuring upper atmospheric water vapor, atomic hydrogen, winds and PMCs, providing by far the most comprehensive description of the shuttle plume-to-PMC phenomenon to date. We regard PMCs as the satellite-observed equivalent of noctilucent clouds (NLCs) and we use the two terms interchangeably. In this work, we analyze for the first time the observed properties of the bright shuttle-produced PMCs, which were detected on the day following launch by satellite and ground-based instruments within 10 min of each other. We simulate the cloud formation using a one-dimensional microphysical model initialized with expected plume water vapor concentrations and quantitatively compare the results to the observations.

[6] We divide this work into ten sections. Section 2 describes the STS-135 launch, sections 3–6 describe the satellite and ground-based observations of the shuttle plume in the days immediately following the launch, sections 7 and 8 describe the bright satellite and ground-based PMC observations on 9 July 2011, section 9 discusses the plume transport in the context of satellite wind observations on 8 July as well as modeling results of the shuttle PMCs, and section 10 summarizes the major findings and suggests topics for future study.

2. The STS-135 Launch

[7] On 8 July 2011 at 15:29 UT, the space shuttle Atlantis launched from the Kennedy Space Center on a mission to the International Space Station. Atlantis followed an ascent trajectory very similar to previous launches [e.g., *Meier et al.*, 2011] and was placed into an orbit with an inclination of 51.6°. As shown in Figure 1a, the shuttle flew nearly horizontally between 100 and 110 km altitude for a significant portion of its ascent as its three main engines injected 350 t of nearly pure water vapor into the lower thermosphere off the east coast of the United States. The lower thermospheric injection of water occurred at 10:30 local solar time (15:35 UT) and was distributed from 31 to 37°N and 71 to 79°W (Figure 1b). We follow the horizontal transport of this plume with five different satellite and ground-based experiments, starting with the Sounding of the Atmosphere using Broadband Emission Radiometry (SABER) instrument on NASA's Thermosphere Ionosphere Mesosphere Energetics and Dynamics (TIMED) satellite.

3. The SABER Observations: Earliest Detection of the STS-135 Main Engine Plume

[8] *Siskind et al.* [2003] reported detections of space shuttle main engine exhaust using the SABER water vapor channel at 6.8 μm and presented 13 plume limb scans over four separate launches in 2002. Using a detection algorithm similar to *Siskind et al.*, we now have assembled over 100 SABER limb scans of shuttle main engine plumes. The complete database of SABER plume observations will be
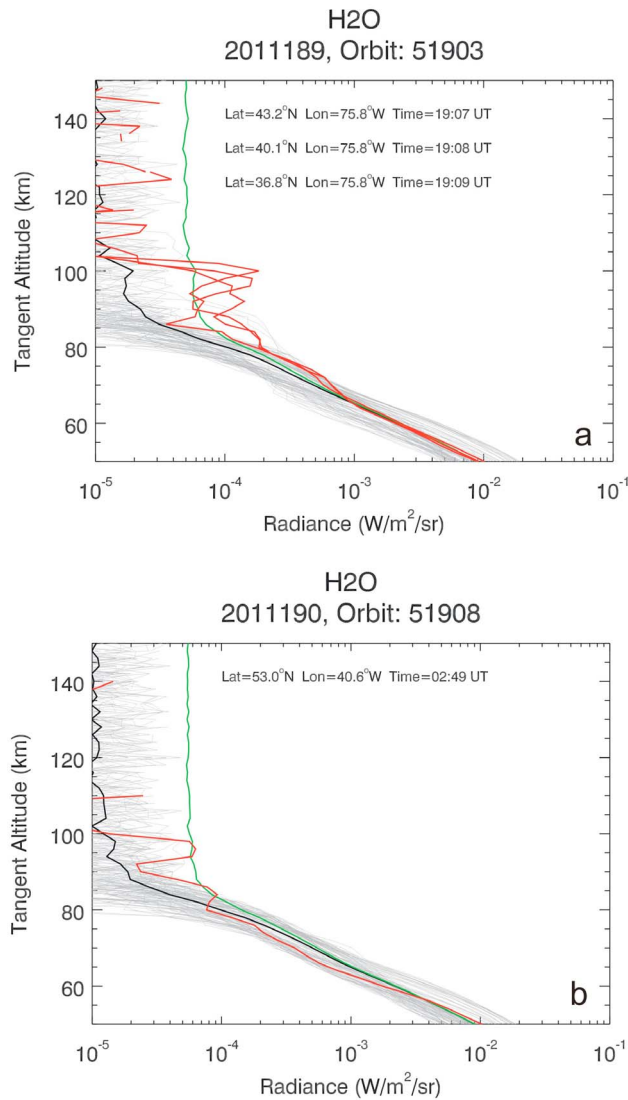
H2O
2011189, Orbit: 51903

Lat=43.2°N Lon=75.8°W Time=19:07 UT

Lat=40.1°N Lon=75.8°W Time=19:08 UT

Lat=36.8°N Lon=75.8°W Time=19:09 UT

Tangent Altitude (km)

Radiance (W/m^2/sr)

a

H2O
2011190, Orbit: 51908

Lat=53.0°N Lon=40.6°W Time=02:49 UT

Tangent Altitude (km)

Radiance (W/m^2/sr)

b

other peak plume emission rates observed by SABER [e.g., *Siskind et al.*, 2003], which exhibit a spread in apparent tangent altitudes ranging from 90 km to 110 km, with a mean of 98 km. Although these values are mostly lower than the water vapor injection heights, they can be explained by the likelihood that plumes are usually not located at the tangent point, but rather in the foreground or background along the SABER line-of-sight. These locations introduce geometric effects that cause the plume to appear lower than its true height, as described in the Appendix. An average drop of 7 km in the apparent peak emission altitude is a consequence of the geometry. The actual displacement distance of the plume from the tangent point and physical effects such as vertical diffusion will modify this average. Still the geometric effect is very close to the mean of the SABER observations and is the likely explanation for the lower observed values. A more comprehensive discussion of the SABER data, including plume radiance heights will be presented in a future publication.

[10] Figure 2b shows another plume detection the next day on 9 July 2011 and the nighttime observation shows that it is at 53°N. The location of all the SABER plume observations used herein are indicated in Figure 1b and listed in Table 1. Note that after only 11.2 h, the plume water vapor is already more than halfway to the Arctic from its point of injection. We next consider observations from the Global Ultraviolet Imager (GUVI) which is also on board the TIMED satellite.

4. The GUVI Observations: The Plume Splits

[11] GUVI has operated in spectral stare mode since December 2007, with a fixed view direction about 40° from the nadir [*Meier et al.*, 2011]. The GUVI entrance slit is divided into 14 separate observing pixels, each covering about 7 km × 7 km when viewing in the nadir. The full field-of-view is therefore about 100 km wide. Each pixel obtains a full spectrum consisting of 176 wavelength elements

Figure 2. (a) SABER observations of the STS-135 plume on 8 July 2011 showing radiance profiles at 6.8 μm (red) 3.6 h after injection of the plume. The gray lines represent all scans from TIMED orbit 51903 and the green line indicates the 4σ threshold from which the plume is identified. Three plume scans are detected in this orbit. (b) Same as Figure 2a except for TIMED orbit 51908, during which one plume detection is identified 11.2 h after plume injection.

presented in a future publication, but for this work we only show the detections of the STS-135 plume.

[9] Figures 2a and 2b show SABER water vapor radiance scans from two different TIMED orbits. As in previous work, the shuttle plumes are identified by their large radiances in the 6.8 μm channel above 90 km altitude, where the background water vapor radiance is typically near the noise level. Figure 2a highlights three sequential daytime plume detections between 19:07 and 19:09 UT on 8 July 2011, only 3.6 h after plume injection. All three scans were near 40°N and 76°W, just north of the shuttle ground track indicated in Figure 1b. The peak altitude of the plume emission is on average at 96.5 km, which is lower than the altitude at which most of the plume is injected (Figure 1a). This is also true of

Table 1. Summary of STS-135 Plume Observations

	Latitude	Longitude	UT (DOY/hh:mm)	dt (hh:mm)	LT (h)
STS-135[a]	31–37 N	71–79 W	189/15:33–15:37	–	10.5
SABER H$_2$O	40 N	76 W	189/19:08	3:33	14.1
GUVI H	37 N	72 W	189/20:13	4:38	15.4
SMR H$_2$O (2)[b]	34 N	76 W	190/23:24	7:49	18.3
SABER H$_2$O	53 N	41 W	190/02:49	11:14	0.1
SMR H$_2$O (8)[b]	18–53 N	31–63 W	190/09:36	18:01	6.9
CIPS PMCs	70 N	24 E	190/12:04	20:29	13.7
RMR NLCs	69 N	16 E	190/12:14	20:39	13.3
SMR H$_2$O (12)[b]	24–59 N	77–12 W	190/20:20	28:45	18.1
MISI H$_2$O	54 N	12 E	190/23:01	31:26	23.8
SMR H$_2$O (9)[b]	28–46 N	16–11 W	191/07:58	41:23	7.1
SMR H$_2$O (19)[b]	23–59 N	56 W–41 E	191/18:46	51:11	18.2
cWASPAM1 H$_2$O	69 N	16 E	191/19:29	51:54	20.5
SMR H$_2$O (12)[b]	2–63 N	21 W–45 E	192/06:27	62:52	7.1
SMR H$_2$O (11)[b]	3–58 N	48 W–81 E	192/17:16	73:41	18.1
SMR H$_2$O (5)[b]	24–52 N	5 E–37 E	193/04:55	85:21	7.0

[a]Launch was at 15:29 UT and the H$_2$O plume was injected between 100 and 110 km. Latitudes and longitudes are indicated over the ground track above 100 km altitude and before main engine cutoff (Figure 1a).

[b]Numbers of SMR scans in excess of 30 K brightness temperature at 99 km are indicated in parentheses and range of latitudes and longitudes are from these detections. UT, dt and LT are from the middle of these scans as measured sequentially in elapsed time.
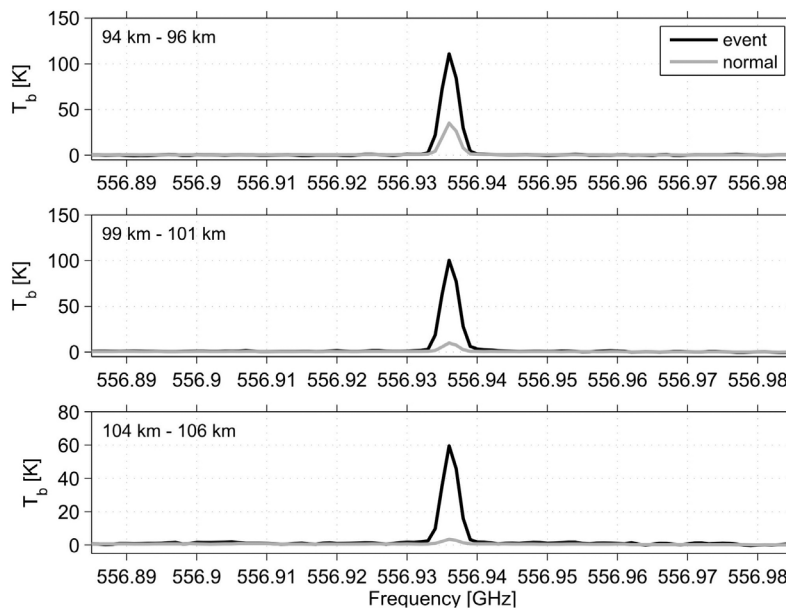
Figure 3. SMR spectra at three different altitudes showing averaged shuttle plume detections (black) relative to the normal signal in the absence of a shuttle plume (gray). The shuttle plume spectrum is an average of about 50 scans over 11 different shuttle launches observed between 2002 and 2010. The normal spectrum is an average over about 3000 scans from global observations all within three days of the 11 shuttle launches.

between 115 and 180 nm, and a spectrum is obtained every 3 s. Spectral data are also reported in the imaging mode format, which consists of five wavelength channels. The GUVI H Lyman-α channel measures wavelengths between 119.3 and 123.6 nm and we use this channel in imaging mode to search for the STS-135 plume, which produces the backscattered emission from photodissociated water vapor [*Stevens et al.*, 2005a; *Meier et al.*, 2010, 2011].

[12] GUVI has produced many images of shuttle plumes during the daytime and a few at night. The plumes are only present in the Lyman-α channel, which requires the removal of the strong underlying Lyman-α airglow for optimal identification, which we do with an orbit of GUVI data that does not contain the plume detection. GUVI detected the STS-135 exhaust plume on 8 July 2011. As shown in Figure 1b the plume signal displays two distinct peaks observed 4.6 h after launch, both with column emission rates near 3.5 kR and a minimum between the peaks with an emission rate near 1 kR. We note that Lyman-α emission from the Earth's disk is typically smooth and unstructured [*Rairden et al.*, 1986; *Bishop*, 1999] so that for a typical daytime background radiance of 40 R, residual radiances following the removal of the background are less than 1 R [*Meier et al.*, 2011]. The visible edges of the plume in Figure 1b about 1400 km apart, indicating very rapid horizontal spreading or shearing at an average speed of 42 m/s from the center to the edge. The rapid spreading/transport of the plume with time is discussed further in the next section.

5. The SMR Observations: Global Scale Plume Transport

[13] In order to track the plume for the time period following detections by GUVI and SABER, we now turn to water vapor observations from the Sub-Millimeter Radiometer (SMR) on the Odin satellite. Odin was launched on 20 February, 2001 into a polar sun-synchronous orbit. The SMR instrument measures thermal emissions on the limb in several frequency bands between 486 GHz and 581 GHz and also near 119 GHz, with an effective spectral resolution of 2 MHz [*Frisk et al.*, 2003]. Information on water vapor in the mesosphere and lower thermosphere (MLT region) is derived from observations near 557 GHz that include a strong water vapor emission line centered at 556.936 GHz. Measurements of this band typically cover the altitude range from 7 km to 110 km every 2.3 min with vertical sampling of 3 km. The instrument's projected field of view is ~1.6 km × 1.6 km (full-width at half-maximum [*Urban et al.*, 2007]) at the tangent point while the horizontal resolution is about 400 km, defined as the path length in a given tangent height layer. Details of the SMR water vapor retrieval in the MLT region and early results are reported by *Lossow et al.* [2007, 2009] and references therein.

[14] Figure 3 shows averaged SMR water vapor spectra. The plume spectrum shown is an average of about 50 spectra between 8 and 61 h from plume injection compiled from 11 different shuttle launches. The normal case is an average of about 3000 spectra from global observations within three days of each of the 11 shuttle launches. The three panels show three different 2 km altitude layers in which spectra were averaged between 94 and 106 km and where the signal from the shuttle plume is the strongest. The plume signal is clearly evident in all three examples and is well above the normal water vapor signal. To locate the STS-135 shuttle plume in latitude and longitude, we focus on the tangent altitude of 99 km, where the brightness temperatures from the plume are high and the background water vapor signal is low. We show the brightness temperatures at the reported altitude of 99 km throughout this work, and inspection of the
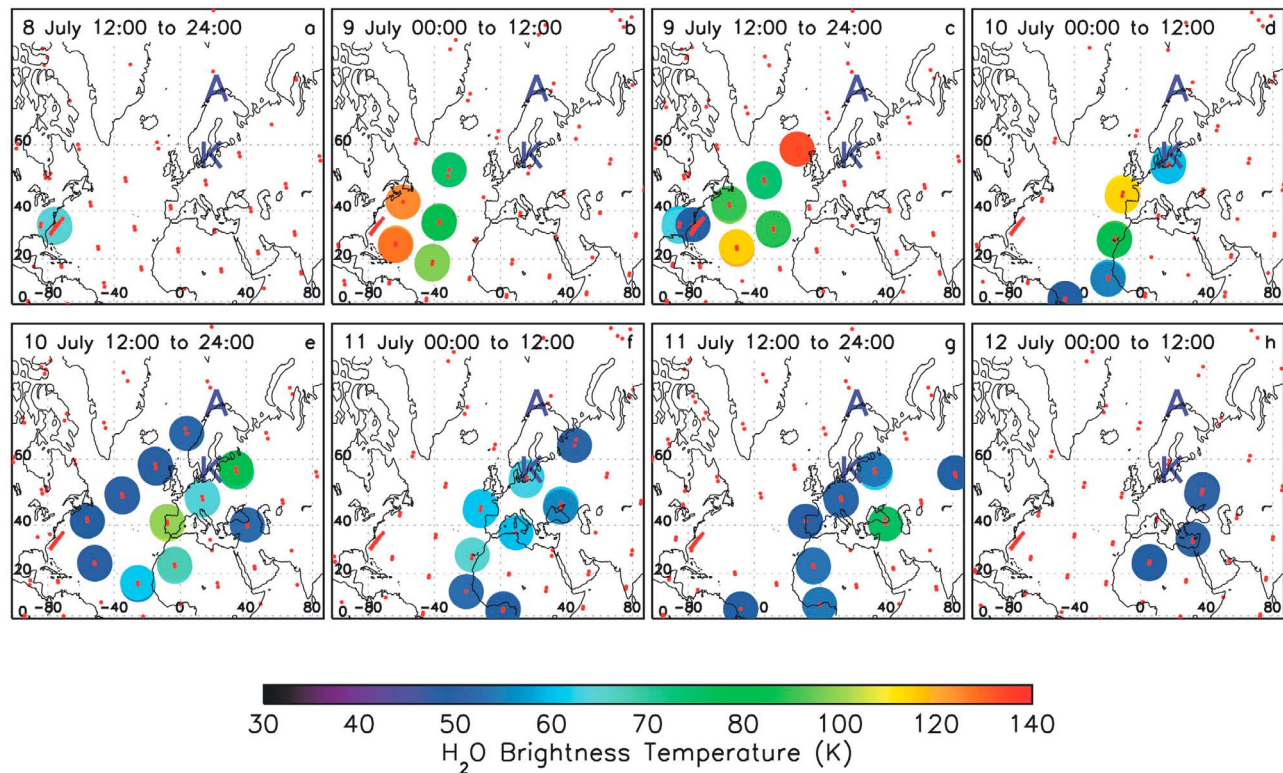
Figure 4. (a–h) Time series of SMR STS-135 main engine plume observations in July, 2011 at 99 km tangent altitude. Each panel assembles 12 h of observations (in UT), so the eight panels represent the four day period immediately following launch. All panels show average brightness temperatures for the frequency band between 556.934 and 556.938 GHz. The STS-135 ground track is shown as the red line off the U.S. east coast, and locations of SMR scans are shown by small red symbols. Only plume detections above the 30 K (3σ) threshold are shown with larger colored symbols, which are enlarged relative to the distance sampled by SMR for clarity. The letter "A" indicates the location of ALOMAR and "K" indicates the location of Kühlungsborn, where identical ground based water vapor instruments were operating during this time period.

SMR water vapor data shows that this altitude most clearly illustrates the motion of the plume. Consideration of a 7-km low bias (see Appendix) yields an altitude of 106 km that is moreover consistent with the main altitudes of plume injection shown in Figure 1a. At the reported plume altitude of 99 km the 3σ detection threshold for a plume signal is about 30 K in July. This threshold is based on an average over the frequency range between 556.934 and 556.938 GHz, which is calculated from a climatology of observations assembled from all latitudes.

[15] Figures 4a–4h show a time series of SMR plume detections at 99 km following launch of STS-135. Because of the small size of the plume relative to the SMR line of sight, it is very difficult to derive reliable local water vapor mixing ratios from the observations; so we instead show the brightness temperatures to identify the plume locations. Local water vapor mixing ratios are discussed further in section 9 where we model the plume to simulate the observed PMCs. Since SMR can measure on either node of the Odin orbit, we assemble all the observed brightness temperatures in eight 12-h increments over four days. There are other detections after the end of this time series but attribution of a plume detection to the shuttle and not another launch vehicle becomes difficult after four days. The first panel shows data on 8 July between 12:00

and 24:00 UT and indicates two detections very close to each other about eight hours after launch. All SMR plume detections for the geographic region indicated in Figure 4a–4h are listed in Table 2.

[16] The next panel (Figure 4b) shows the data on 9 July between 00:00 and 12:00 UT, where several detections over 30 K are made over the Atlantic Ocean. The most northerly detection is at 53°N with a brightness temperature of 79 K observed at 9:26 UT, about 18 h after plume injection. The maximum detected brightness temperature for this time period is 129 K at 26°N and 63°W, and parts of the plume are observed at latitudes as low as 18°N. The horizontal extent of the shuttle plume in Figure 4b is remarkable, extending about 4000 km from southwest to northeast and about 3000 km from northwest to southeast. This is over two orders of magnitude larger than the calculated full width of the water vapor plume with or without eddy mixing included (10 to 20 km [*Meier et al.*, 2011]). Thus the rapid plume spreading is not only reflected in the GUVI H Lyman-α observations after 5 h (Figure 1b) but also the SMR water vapor observations after 18 h.

[17] Figures 4c–4h show the six remaining 12 h intervals of the plume evolution, where it splits into two primary sections at the end of 9 July (Figure 4c) and continues to

Table 2. SMR STS-135 Main Engine Plume Detections

GMT	dt (hh:mm)[a]	Latitude	Longitude	LT	T(K)
189/23:24:05	07:49	33.5	284.2	18.3	63.0
189/23:24:25	07:49	34.8	283.9	18.3	60.1
190/09:26:23	17:51	53.4	329.1	7.4	78.9
190/09:31:07	17:56	36.1	323.2	7.1	95.2
190/09:31:23	17:56	35.1	322.9	7.0	88.5
190/09:35:47	18:01	18.8	319.0	6.9	101.9
190/09:36:07	18:01	17.6	318.7	6.9	102.5
190/11:05:29	19:30	43.1	301.2	7.2	126.6
190/11:09:52	19:35	27.0	296.8	6.9	124.3
190/11:10:08	19:35	26.0	296.5	6.9	129.2
190/12:43:56	21:09	35.2	274.8	7.0	54.3
190/12:44:16	21:09	33.9	274.4	7.0	57.5
190/18:46:26	27:11	59.0	345.9	17.8	134.1
190/20:15:29	28:40	32.4	331.6	18.4	89.4
190/20:15:45	28:41	33.3	331.3	18.4	94.8
190/20:20:13	28:45	49.8	326.2	18.1	77.1
190/20:20:29	28:45	50.8	325.8	18.1	77.6
190/21:49:36	30:15	24.3	309.5	18.5	123.3
190/21:49:52	30:15	25.4	309.2	18.4	118.2
190/21:54:16	30:19	41.6	304.9	18.2	101.7
190/21:54:32	30:20	42.6	304.6	18.2	96.0
190/23:28:39	31:54	39.0	282.9	18.3	31.8
191/06:17:35	38:43	55.3	17.1	7.4	55.5
191/06:17:51	38:43	54.3	16.6	7.4	51.9
191/07:56:18	40:21	46.4	349.3	7.2	114.8
191/07:56:38	40:22	45.2	348.9	7.2	117.2
191/08:01:02	40:26	29.0	344.3	7.0	97.2
191/08:01:18	40:26	28.1	344.1	7.0	88.4
191/08:05:46	40:31	11.5	340.4	6.8	53.4
191/08:06:02	40:31	10.5	340.2	6.8	42.8
191/09:44:48	42:10	1.3	314.3	6.7	33.6
191/15:33:02	47:58	40.1	40.6	18.3	39.3
191/15:37:34	48:03	56.8	34.1	17.9	75.2
191/15:37:50	48:03	57.8	33.6	17.9	84.9
191/17:11:38	49:37	48.7	13.6	18.1	62.7
191/17:11:54	49:37	49.8	13.2	18.1	59.6
191/17:16:18	49:44	65.7	4.0	17.5	37.4
191/18:41:00	51:06	23.1	356.8	18.5	60.6
191/18:41:16	51:06	24.2	356.6	18.5	66.0
191/18:45:40	51:11	40.5	352.4	18.3	107.5
191/18:45:56	51:11	41.4	352.1	18.2	104.8
191/18:50:24	51:15	57.8	345.4	17.9	34.6
191/18:50:40	51:16	58.8	344.9	17.8	31.4
191/20:15:03	52:40	14.9	334.5	18.6	43.2
191/20:15:19	52:40	15.8	334.3	18.5	53.6
191/20:24:27	52:49	49.6	325.1	18.1	36.5
191/20:24:43	52:50	50.6	324.8	18.1	35.5
191/21:53:52	54:19	24.2	308.4	18.5	33.5
191/21:54:04	54:19	24.9	308.2	18.5	31.5
191/21:58:32	54:24	41.5	303.9	18.2	32.8
192/04:43:22	61:08	63.3	44.9	7.7	36.6
192/04:47:46	61:13	47.4	36.7	7.2	54.3
192/04:48:02	61:13	46.4	36.4	7.2	44.8
192/06:21:49	62:47	55.5	16.1	7.4	55.1
192/06:22:05	62:47	54.5	15.6	7.4	57.7
192/06:26:49	62:52	37.2	9.4	7.1	52.3
192/06:35:57	63:01	3.4	1.8	6.7	39.9
192/06:36:13	63:01	2.4	1.6	6.7	32.4
192/08:00:34	64:26	46.5	348.3	7.2	53.6
192/08:00:54	64:26	45.3	347.9	7.2	53.3
192/08:05:34	64:31	28.1	343.0	7.0	60.7
192/08:10:02	64:35	11.6	339.4	6.8	39.9
192/12:29:13	68:54	56.6	81.3	17.9	31.8
192/15:37:23	72:02	40.5	39.4	18.3	79.3
192/15:41:47	72:07	56.6	33.2	17.9	55.9
192/15:42:03	72:07	57.6	32.6	17.9	41.8
192/17:15:53	73:41	48.6	12.6	18.1	36.7
192/17:16:09	73:41	49.6	12.2	18.1	37.2
192/18:40:30	75:06	5.4	359.5	18.6	41.7
192/18:45:14	75:10	22.9	355.8	18.5	43.0
192/18:45:30	75:10	23.9	355.5	18.5	43.0
192/18:50:14	75:15	41.4	351.0	18.2	31.0

Table 2. (continued)

GMT	dt (hh:mm)[a]	Latitude	Longitude	LT	T(K)
192/21:52:31	78:18	3.3	311.7	18.7	32.5
193/04:50:48	85:16	51.9	37.4	7.3	34.5
193/04:51:08	85:16	50.7	36.9	7.3	36.6
193/04:55:32	85:21	34.6	31.7	7.0	36.6
193/06:34:20	86:59	25.3	5.4	6.9	33.3
193/06:34:36	87:00	24.4	5.1	6.9	33.7

[a]Time from plume injection at 189/15:35 UT. All plume detections for 99 km altitude and for the geographic region shown in Figures 4a–4h.

move eastward until 12 July (Figure 4h). On 9 and 10 July (Figures 4c–4e) the plume is moving across Europe where there are identical ground-based instruments capable of measuring upper atmospheric water vapor in Germany and Norway. These observations are discussed next.

6. Ground-Based Water Vapor Observations: The Plume Arrives at High Latitudes

[18] The MIcrowave Spectrometer at the Institute of Atmospheric Physics (MISI) instrument has been measuring upper atmospheric water vapor from Kühlungsborn, Germany (54°N, 12°E) since 2010. This microwave instrument measures at frequencies near 22.235 GHz and details of the instrument and the water vapor retrievals are given by *Hallgren and Hartogh* [2012]. We assemble microwave spectra from three consecutive 20 min observations in Figure 5, starting at 22:31 UT. This time period corresponds to the SMR observations between Figures 4c and 4d during which part of the plume is very near Kühlungsborn. The length of the integration time is selected based on previous microwave observations of the STS-85 shuttle main engine plume reported by *Stevens et al.* [2003] and measured by the WASPAM instrument operating at ALOMAR until 2008 [*Hartogh et al.*, 2010]. The upper panel shows the first 20 min timestep where there is no plume, the middle panel includes data when the plume is overhead, and data in the lower panel cover the next time step when the plume has already passed over. Each panel also shows an average atmospheric background spectrum for all observations from July, 2011.

[19] In the middle panel of Figure 5 an elevated brightness temperature at line-center is present with a total brightness temperature excursion of 0.2185 K (218.5 mK) at $23:01 \pm 00:10$ UT. This signal was determined by subtracting the mean and fitting a polynomial to the spectrum and is 3.1σ above the variability within the spectrum shown. The noise in the MISI spectra is relatively high due to the short integration time required for the rapidly moving shuttle plume. Nonetheless, the large positive spike is at the expected time suggested by the satellite data in Figure 4. As discussed in *Stevens et al.* [2003], these data are consistent with a main engine shuttle plume appearing as a transient, bright and narrow feature in the center of the emission spectrum where the high altitude water emission is purely Doppler broadened. The frequency and magnitude of the signal in the middle panel of Figure 5 is generally consistent with that reported from the STS-85 plume by *Stevens et al.* [2003].
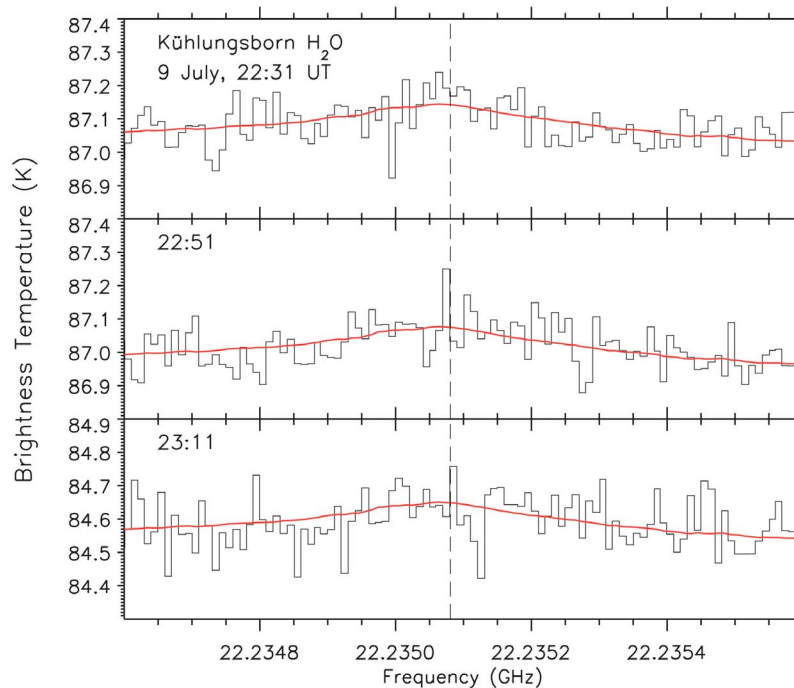
Figure 5. Three sequential 20 min observations of water vapor from the MISI instrument in Kühlungsborn, Germany (54°N, 11°E) the day after launch of STS-135. The red curve is the July 2011 average scaled to the emission feature in each panel. The narrow feature in the center of the middle panel is 3.1σ above the background and indicates passage overhead of the STS-135 main engine plume where the center frequency is indicated by the dashed line. The time period corresponds to the SMR satellite observations between Figures 4c and 4d.

[20] We note that because of the narrowness of the feature (i.e., no pressure broadening from the background atmosphere to provide an altitude estimate), we can only state that it originates above 85 km altitude. The MISI field of view projected to the lower thermosphere is 13 km × 26 km. The total number of water vapor molecules that produce the plume signal is 1×10^{28} or about 0.1% of the lower thermospheric main engine plume initially injected. If these molecules are uniformly distributed over a 2.5 km layer at 105 km altitude then the transient plume water vapor mixing ratio over Kühlungsborn at that altitude is 4000 ppm.

[21] An analysis of all MISI spectra from July 2011 reveals that the probability of a signal greater than 2.8σ above the mean at any frequency bin is only 0.2%, so the detection in the middle panel of Figure 5 is robust. Nonetheless, we note two issues for which we have no explanation. The plume signal detected by MISI only appears in one polarization rather than both and also in only one frequency bin, whereas our calculations indicate that it should appear in two. The arrival of the plume in Kühlungsborn on 9 July is 31 h following launch, implying an average northward speed of 20 m/s during this time.

[22] The cWASPAM1 water vapor instrument is at the Arctic Lidar Observatory for Middle Atmospheric Research (ALOMAR) in Andenes, Norway (69°N, 16°E) and is identical to the MISI instrument. In Figure 6 we assemble the data in a similar way for a one-hour time period on 10 July starting at 18:59 UT. This time period corresponds to the SMR observations between Figures 4e and 4f during which part of

the plume passes near ALOMAR. Again, the background signal is a July averaged spectrum that is scaled to each data set. Here we find a bright feature in the center of the spectrum showing a brightness temperature increase of 0.369 K (369 mK) at 19:29 ± 00:10 UT, some 3.4σ above the background. Like the MISI spectra in Figure 5, the noise of the cWASPAM1 data is relatively high due to the short integration time but the location and strength of the plume signal is as expected and in the context of the satellite observations in Figure 4 is evidence that the plume was over ALOMAR during the indicated time period.

[23] The cWASPAM1 field of view projected to the lower thermosphere is 67 km × 21 km and the total number of water vapor molecules that produce the cWASPAM1 plume signal is 8×10^{28} or about 0.8% of the lower thermospheric main engine plume initially injected. The arrival of the water vapor plume at ALOMAR on 10 July is 52 h after deposition of the water vapor, implying an average northward speed of 21 m/s during that time, nearly identical to the northward speed inferred from Kühlungsborn the day before (20 m/s).

[24] Taken together, the four water vapor data sets (SABER, SMR, MISI and cWASPAM1) and the H Lyman-α data set (GUVI) presented in section 3–6 reveal rapid spreading and rapid northeastward transport of at least part of the shuttle's main engine water vapor exhaust, with a northernmost plume detection latitude of 69°N. We next consider unusually bright PMCs on 9 July. We present satellite observations from the Cloud Imaging and Particle Size (CIPS) instrument on the
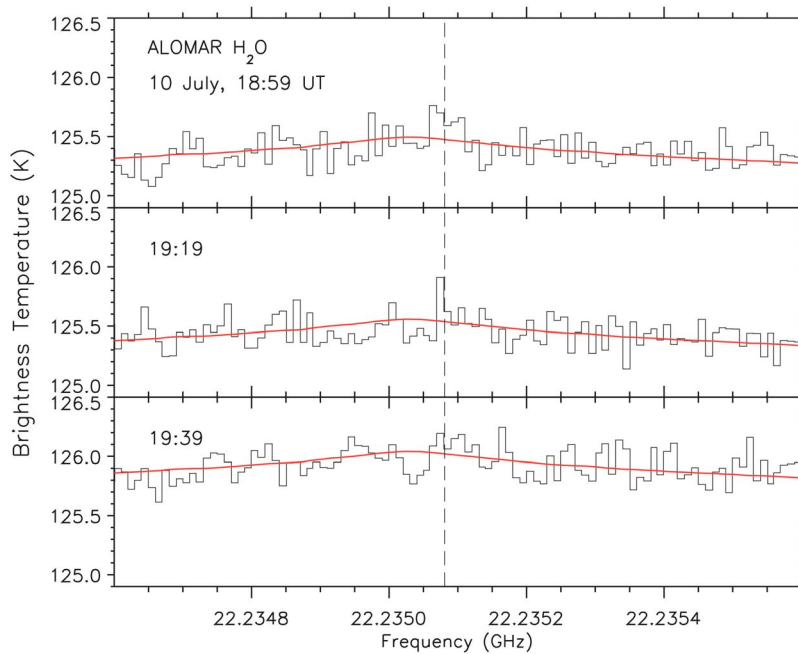
Figure 6. Three sequential 20 min observations of water vapor from the cWASPAM1 instrument in Andenes, Norway (69°N, 16°E). The red curve is the July 2011 average scaled to the emission feature in each panel and the center frequency is indicated by the dashed line. The narrow feature in the center of the middle panel is 3.4σ above the background and indicates the passage of the STS-135 plume.

Aeronomy of Ice in the Mesosphere (AIM) satellite and ground-based lidar observations at ALOMAR.

7. CIPS Observations: Bright PMCs in the Arctic on 9 July

[25] Since it is well known that increases in water vapor strongly affect PMC ice particle growth and cloud brightness [e.g., *Rapp and Thomas*, 2006], we searched for variations of the brightest PMC population following the STS-135 launch. This approach was used in previous studies identifying the impact of shuttle launches using the Solar Backscatter Ultra-violet (SBUV) suite of instruments [*Stevens et al.*, 2005a, 2005b; *Collins et al.*, 2009], which indeed are only sensitive to the brightest PMCs [e.g., *Shettle et al.*, 2009]. In this section, we compare increases of this population immediately after the shuttle launch to a longer time series to determine whether bursts of bright PMCs appear preferentially after the exhaust was deposited into the upper atmosphere. Here we use data from the CIPS instrument on the AIM satellite and consider the variation of the brightest CIPS clouds.

[26] The AIM satellite was launched on 25 April, 2007 into a sun-synchronous, 97° inclination orbit and has since measured PMCs over the Arctic and Antarctic in the summertime nearly continuously [*Russell et al.*, 2009]. CIPS images PMCs by measuring scattered sunlight at 265 nm while viewing toward the nadir with four different cameras arranged in a field of view that is 120° × 80° (2000 km × 1000 km) [*Benze et al.*, 2009; *McClintock et al.*, 2009]. PMCs can be distinguished from the underlying Rayleigh scattered background by measuring the phase function of the solar scattered light over several different scattering angles at each location [*Bailey et al.*, 2009] with a spatial resolution of 5 km × 5 km. The

latest public release of the CIPS data (Version 4.20), which we use herein, contains PMC frequency, directional albedo, ice particle size and ice water content (IWC).

[27] CIPS was operating routinely during and after the STS-135 launch, measuring cloud properties near 14:00 LT on the descending node of each orbit at 70°N. Figure 7 is a four panel image of CIPS albedos observed on each day from 8 to 11 July 2011. Albedo values are normalized to a solar scattering angle of 90°; the normalization uses a particle phase function that is constrained by the lidar data described by *Baumgarten et al.* [2010] and assumes that particles have an axial ratio of two and a distribution width that varies as half the particle radius. There is a prominent burst of bright PMCs on 9 July that is not apparent the day before or on either of the two days after. The brightest PMCs observed equatorward of 71°N on 9 July is at 70°N and 24°E with an albedo of 48×10^{-6} sr^{-1}, seven times larger than the average CIPS PMC albedo between 69 and 71°N for the week before the launch. This albedo has a derived ice particle radius of 52 nm, which is generally consistent with the rest of the CIPS observations. We discuss particle sizes further in section 8 when we present the vertical profile of ice particle radii.

[28] In order to put these CIPS clouds into context with the rest of the PMC season, we assemble a time series of bright clouds in Figure 8. Here we totaled the number of PMCs brighter than 27×10^{-6} sr^{-1} on each day throughout the season from 64 to 72°N. Figure 8 shows that there is a large burst of bright clouds on day 190 (9 July), suggesting that the clouds near ALOMAR in Figure 7 on that day are indeed unusual.

[29] Arrows in Figure 8 indicate times of the STS-135 launch as well as all other large liquid fueled orbital launches worldwide during the northern summer of 2011. Each of the
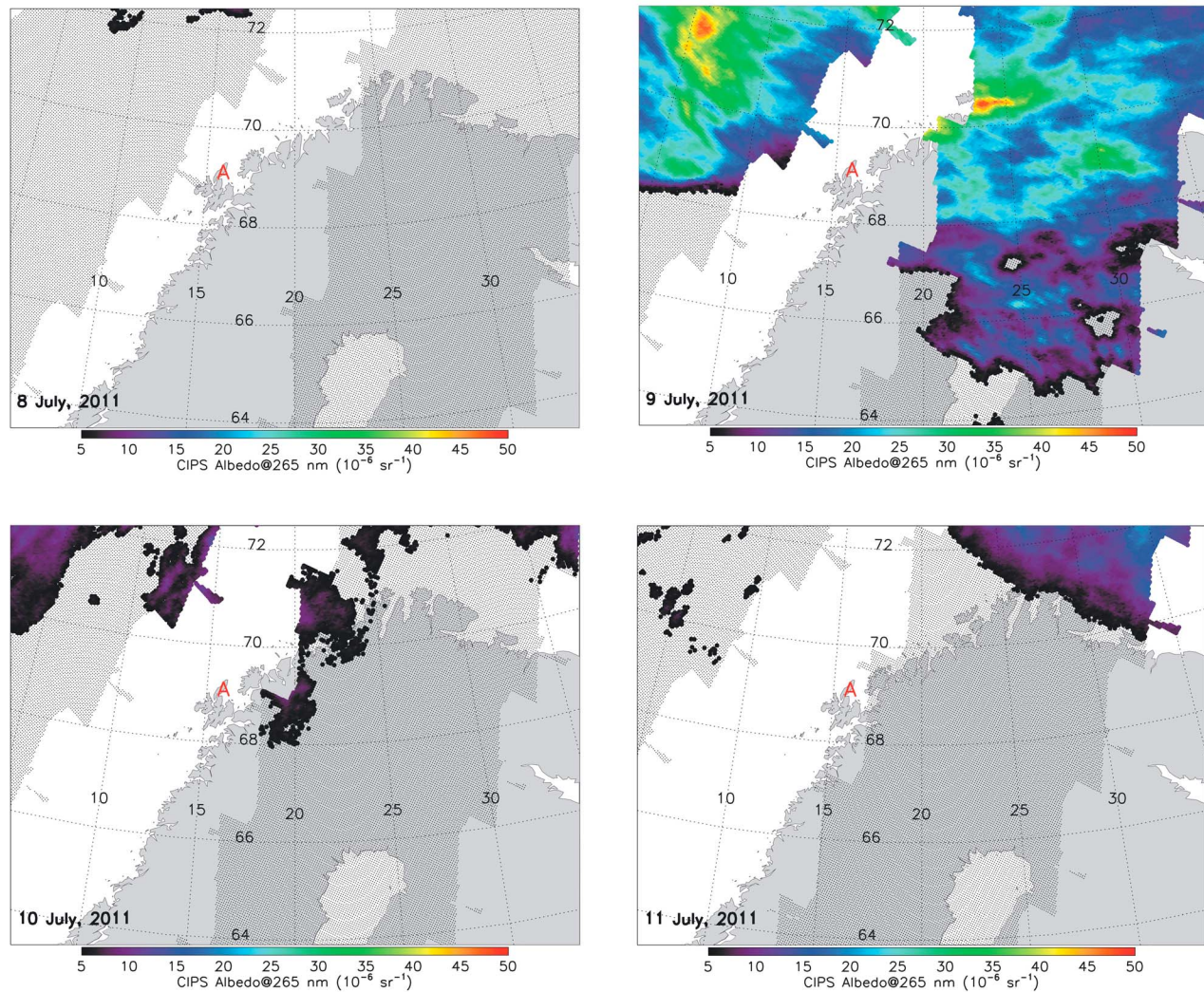
Figure 7. Four panel time series of PMCs observed by CIPS over Scandinavia on the day of the STS-135 launch (8 July) and the three days after launch. The CIPS detection threshold is $2 \times 10^{-6}\,\mathrm{sr}^{-1}$ so the image shows all clouds that are a factor of 2.5 or more above the detection threshold. The "A" indicates the location of ALOMAR (69°N, 16°E), where there are upper atmospheric water vapor observations and ground-based NLC observations. A broad region of bright clouds surrounds ALOMAR on 9 July. Null detections by CIPS are indicated by the stippled region. Note that the field-of-view of CIPS does not sample the region immediately around ALOMAR for the data shown.

launches is listed in Table 3, which includes the gross mass and the propellant mass of each vehicle. The propellant from STS-135 represents about 20% of all liquid propellants in vehicles launched between 6 June and 7 August 2011. Water vapor is a common effluent in liquid fueled launches [e.g., *Kellogg*, 1964] and the water vapor yield from the shuttle's main engines is over 95% by weight [*AIAA*, 1991]. We note that each of the vehicles in Table 3 can have a different propellant combination that can produce other effluents besides water vapor. Relating the contribution of these other vehicles to the northern 2011 PMC production in general requires knowledge of not only the composition of the effluents but also the time and location of the launch, the ascent trajectory and the upper atmospheric winds during each launch. We leave this analysis to future work.

[30] The brightest CIPS clouds on 9 July associated with STS-135 (Figure 8) were observed at 12:04 UT, implying a mean northward speed of 55 m/s for nearly one day (20:29 elapsed time from plume injection, see Table 1). This is slightly faster than average meridional wind speeds previously inferred for shuttle plumes to the Arctic or Antarctic of 31 to 44 m/s [*Stevens et al.*, 2003, 2005a], and several times faster that mean meridional winds derived from satellite wind climatologies for July conditions at 105 km [*Zhang et al.*, 2007]. We now present ground-based NLC observations from ALOMAR during this same time period, which are also highly unusual.

8. RMR Lidar Observations: Properties of Unusually Bright NLCs on 9 July

[31] The Rayleigh/Mie/Raman (RMR) lidar was observing NLCs from ALOMAR (69°N, 16°E) on 9 July 2011. The RMR lidar has been operating since 1997 from this location
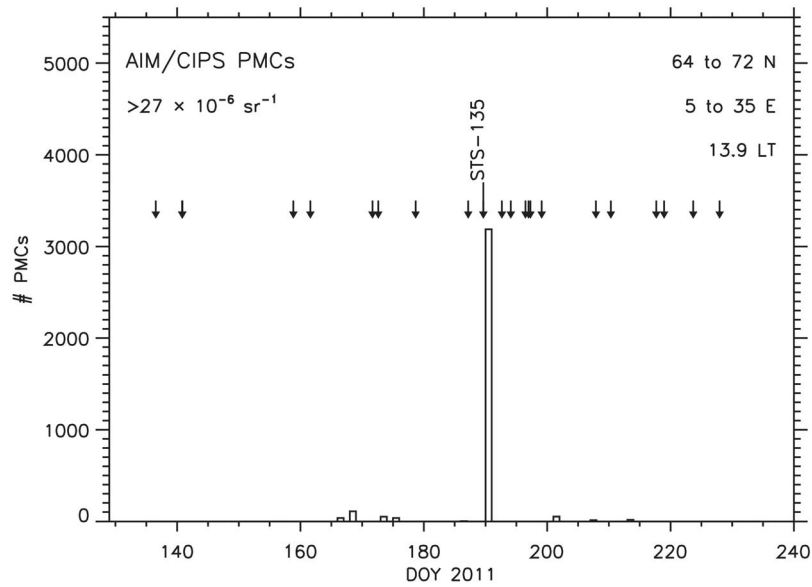
Figure 8. Daily CIPS observations of bright PMCs between 64 and 72°N in 2011 from the descending node of the AIM orbit. The brightness threshold used is 27×10^{-6} sr^{-1}, representing less than 1% of the PMCs for the northern 2011 season. The spike on day of year (DOY) 190 (9 July) is observed the day after launch of STS-135. Also indicated are days during which liquid fueled rockets were launched worldwide (arrows, see Table 3). STS-134 was launched on DOY 136 (16 May), before the start of the PMC season.

and is capable of observing the vertical structure of NLCs and their properties throughout the diurnal cycle by measuring photons backscattered from NLC particles at three laser wavelengths: 1064, 532 and 355 nm. Details of the measurements and a database of results are given in *Baumgarten and Fiedler* [2008] and *Fiedler et al.* [2011].

[32] Figure 9 shows the volume backscatter coefficient $\beta(z,t)$ at 532 nm for a 4-h period on 9 July between 11:00 and 15:00 UT. Between 11:57 UT and 12:18 UT β was unusually

high, with a peak (β_{max}) of 3.9×10^{-9} m^{-1} sr^{-1} when averaged over 20 min. The maximum in Figure 9 is about 5.5×10^{-9} m^{-1} sr^{-1} when using two minute averages. We note that this bright cloud appears at the same time CIPS observed unusually bright PMCs nearby (12:04 UT, Figure 7). This value of β_{max} is about five times larger than the 15-year average for all NLC detections at ALOMAR (7.4×10^{-10} m^{-1} sr^{-1}) and nearly twice as large as the mean β_{max} for "strong" NLCs, which represent the brightest 16% of all NLCs

Table 3. Orbital Vehicles Launched During the Northern 2011 Summer[a]

Date	DOY	Vehicle	Latitude[b]	Longitude[b]	LT	Gross Mass[c] (t)	Propellant Mass[d] (t)
16 May 12:56	136.5389	Shuttle	28.5	−81.0	7.5	2000	720
20 May 19:15	140.8021	Proton	45.6	63.4	23.5	700	640
20 May 20:38	140.8597	Ariane 5	5.2	−52.8	17.1	700	170
7 June 20:13	158.8424	Soyuz	45.6	63.4	0.4	300	120
10 June 14:20	161.5972	Delta 2	34.7	−120.6	6.3	200	100
20 June 16:13	171.6757	Long March 3B	28.2	102.0	23.0	400	220
21 June 14:38	172.6097	Soyuz	45.6	63.4	18.9	300	120
27 June 16:00	178.6667	Soyuz	62.9	40.8	18.7	300	120
6 July 04:28	187.1867	Long March 2C	41.3	100.3	11.2	200	180
8 July 15:29	189.6451	Shuttle	28.5	−81.0	10.1	2000	720
11 July 15:41	192.6535	Long March 3C	28.2	102.0	22.5	400	220
13 July 02:27	194.1021	Soyuz	45.6	63.4	6.7	300	120
15 July 11:18	196.4708	PSLV	13.7	80.2	16.6	300	190
15 July 23:16	196.9694	Proton	45.6	63.4	3.5	700	640
16 July 06:41	197.2785	Delta 4	28.5	−81.5	1.2	400	220
18 July 02:31	199.1049	Zenit 3 F	45.6	63.4	6.7	500	420
26 July 21:44	207.9056	Long March 3A	28.2	102.0	4.5	200	220
29 July 07:42	210.3208	Long March 2C	41.3	100.3	14.4	200	180
5 Aug 16:25	217.6840	Atlas 5	28.5	−81.5	11.0	500	280
6 Aug 22:53	218.9535	Ariane 5	5.2	−52.8	19.4	700	170
11 Aug 16:15	223.6771	Long March 3B	28.2	102.0	23.0	400	220
15 Aug 22:57	227.9563	Long March 4B	37.8	111.5	6.4	200	230

[a]See http://spaceflightnow.com/tracking/launchlog.html. Only liquid fueled vehicles greater than 100 t gross mass at launch included.
[b]Latitude and longitude of launch site.
[c]To nearest 100 t [*Isakowitz et al.*, 1999].
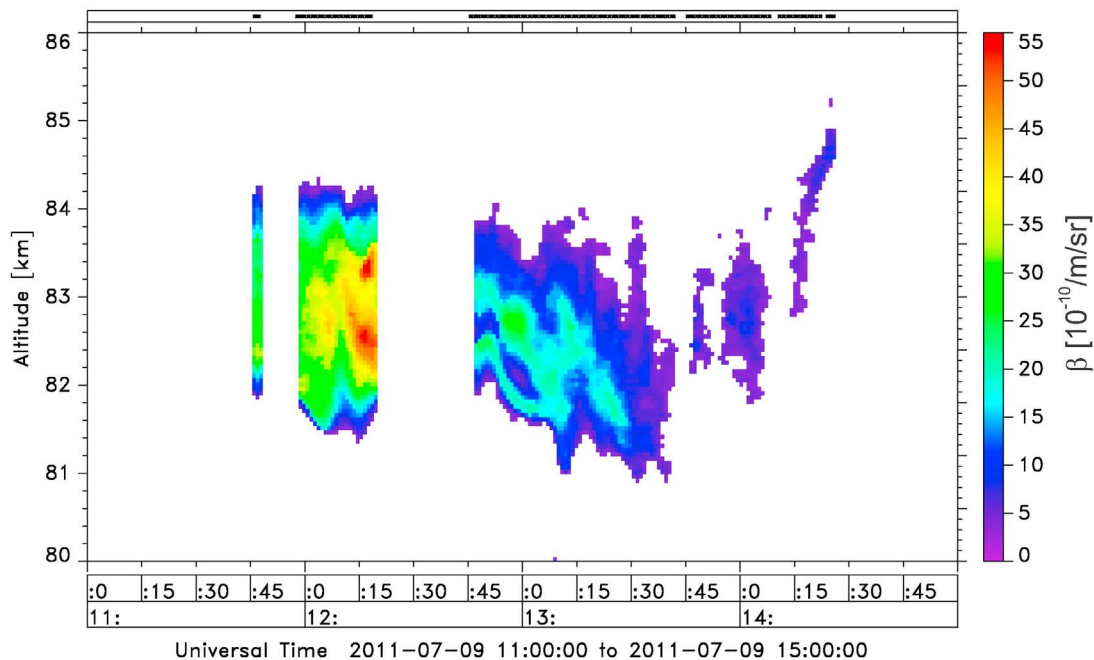[d]Not including boosters and to nearest 10 t [*Isakowitz et al.*, 1999].

Figure 9. Volume backscatter coefficient (β) at 532 nm from the RMR lidar at ALOMAR (69°N, 16°E) for a 4-h period on 9 July 2011. The white spaces at the top of the plot indicate time periods for which there is no data due to tropospheric cloud cover. The bright NLC around 12:15 UT appears 21 h after the shuttle main engine plume was injected.

detected [*Fiedler et al.*, 2011]. The peak altitude of this exceptionally bright cloud is 82.8 km and not particularly unusual compared to the average of 83.3 km calculated from all NLCs.

[33] Although the peak NLC brightness in Figure 9 is unusually high, it also extends vertically over two kilometers so is therefore also unusually thick. The combination of these two attributes sets the event apart from typical NLCs. To quantify its abnormality, we first calculated the total volume backscatter coefficient of the cloud observed between 11:57 and 12:18 UT on 9 July 2011 (β_{int}) to be 77×10^{-7} sr^{-1} by vertically integrating the backscatter coefficient following *Baumgarten et al.* [2012]. Next we computed the backscatter coefficient occurrence frequency from the RMR database since 1997 using 15 min means. This is shown as the histogram in Figure 10. There we see that $\beta_{int} = 77 \times 10^{-7}$ sr^{-1} is about 15 times brighter than the median β_{int} (4.95×10^{-7} sr^{-1}) and brighter than 99.98% of all RMR clouds observed. Clearly this is a highly unusual NLC. Given the proximity of the shuttle plume in space and time from the independent water vapor and PMC observations presented above, this is additional and compelling evidence that this NLC was produced by the STS-135 main engine plume.

[34] Of particular relevance to this study is the vertical structure of the NLC. Figures 11a and 11b display the altitude profile of β shown in Figure 9. Average values of β are shown in both panels and referenced to the top axis. In Figure 11a we also show the ice particle radius as a function of altitude for this unusual cloud compared to the nominal dependence of radius on altitude for all other clouds detected by the RMR lidar since 2006. Although the overall particle sizes of this particular cloud are between 35 and 75 nm and not unusually large compared to typical NLCs, the ice

particles are larger at higher altitudes, in contrast to the mean behavior which has the opposite dependence. In a search through the NLC database from ALOMAR we find that such an inverted size distribution occurs in only 30% of all NLCs observed. In greater contrast to the mean profile is the size of the ice particles between 84 and 84.5 km in Figure 11a. The ice particle radii are greater than 70 nm here, which is the case in only 2% of the NLC in the RMR database of NLC observations.

[35] Figure 11b shows the volume ice density of the cloud, which is larger by about a factor of three compared to the
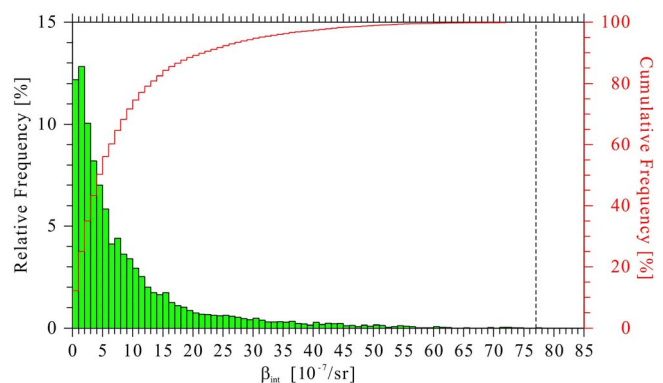

Figure 10. The relative frequency of the vertically integrated volume backscatter coefficient (β_{int}) for all NLC observations by the RMR lidar since 1997. The cumulative frequency (red) shows the percentage of clouds that have a lower β_{int} than that indicated. The unusually bright NLC in Figure 9 has a β_{int} of 77×10^{-7} sr^{-1} (dashed line) and is larger than 99.98% of all RMR clouds observed.
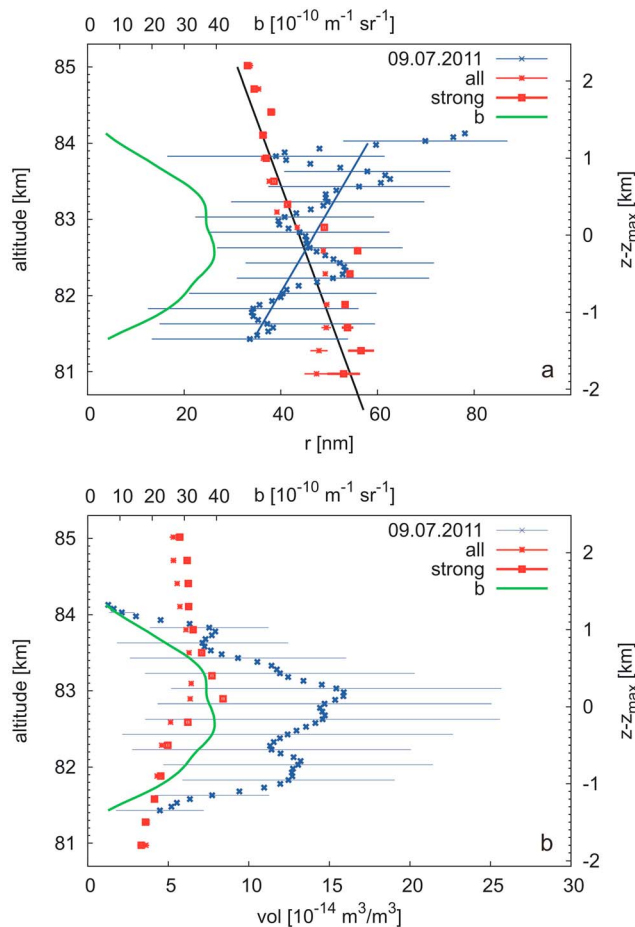
Figure 11. (a) The altitude dependence of the inferred ice particle radius of the NLC observed on 9 July 2001 and averaged between 11:57 and 12:18 UT (blue symbols). The altitude profiles of the mean NLC behavior between 2006 and 2011 inferred from the RMR lidar data for "strong" NLCs and all NLCs at ALOMAR are also shown (red symbols). Best fit straight lines are overplotted and indicate that the particle radius altitude profile for this unusual NLC is opposite to the mean behavior. The average backscatter coefficient at 532 nm ("b") of the unusual NLC is overplotted in green and referenced to the top axis. (b) Same as Figure 11a except showing the volume ice density (vol) of the unusual cloud in blue compared to average NLCs and strong NLCs in red. Note the multiply layered structure with a larger volume density in the upper layer than in the lower layer. The average backscatter coefficient of the unusual cloud is overplotted in green and referenced to the top axis.

mean ice density. Although it is not particularly unusual to observe two layers in an NLC, it is relatively unusual to see higher ice density in the upper layer than in the lower layer. In typical multilayered NLCs, only 36% have a larger ice density in the upper layer.

9. Discussion

[36] The SMR water vapor data show that the plume dispersed rapidly, extending 3000 to 4000 km after only 18 h. We therefore demonstrate for the first time rapid spreading of the plume water vapor and we show this spreading in 12-h increments until four days from launch. This rapid spreading of the plume water vapor to regions extending thousands of km is in contrast to the PMCs formed, which are more localized in space and time (Figures 7 and 9). This is most likely due to the fact that only a small portion of the diffused STS-135 plume reaches the cold summer polar region where PMCs can readily form.

[37] Based on GUVI observations of photodissociated H Lyman-α from a space shuttle plume by *Stevens et al.* [2005a], *Kelley et al.* [2009] argued that the plume diffusion was anomalously fast. However, *Meier et al.* [2010, 2011] also analyzed the Lyman-α observations and found that classical molecular diffusion could explain the shuttle plume expansion up until 10 h from launch, which did not exclude wind shears and turbulent mixing also playing a role throughout the plume lifetime. In this section, we discuss the evidence for strong wind shears in the plume data and we also consider how turbulent mixing can move the lower thermospheric water vapor down to the mesopause where PMCs can form.

[38] An important finding from the ground-based and satellite PMC data is that in order to form the clouds shown in sections 7 and 8 from the STS-135 main engine plume, sustained northward winds of about 55 m/s are required over 21 h. But the water vapor plume was not detected at ALO-MAR until the next day (see Table 1), suggesting a lower meridional transport speed of 21 m/s. Thus it is likely that different parts of the plume are traveling at significantly different speeds indicating global-scale shearing processes, as suggested also by the GUVI H Lyman-α observations in Figure 1b and the SMR time series in Figure 4. A summary of all the plume observations assembled herein is given in Table 1 and a summary of all the SMR plume observations is given in Table 2. The inferred rapid meridional transport underscores the pressing need for a quantitative understanding of lower thermospheric winds and how they control global-scale transport of constituents.

[39] To this end, we have examined wind observations from the Doppler Interferometer (TIDI), which was operating on the TIMED satellite along with GUVI and SABER during the STS-135 mission. Analysis of the entire TIDI data set and rapid meridional winds associated with the STS-107 main engine plume in January, 2003 were reported by *Niciejewski et al.* [2011]. We present herein TIDI wind retrievals which are a Level 3 product as described by *Niciejewski et al.* [2006] and Version 11 (v11) data, which has not been described in the literature heretofore. Previous studies such as *Niciejewski et al.* [2011] have used Version 10 data. V11 contains several improvements over previous analysis: (1) the long-term instrumental drift in TIDI, on the order of 300 m/s over the past 10 years, is removed prior to fitting airglow spectra to ensure that initial guesses for the nonlinear least squares fitting of the spectra are close enough to guarantee convergence; (2) the instrumental contribution to spectra recorded by TIDI continues to slowly change as water vapor sublimates away at a measurable rate – the brightness of the neon spectral calibration lamp increases approximately 2.5%/year requiring weekly updates to airglow spectra analysis, rather than employing the launch calibration; (3) TIDI observes the terrestrial limb airglow with multiple filters tuned for specific tangent altitudes from 65 to 300 km – v11 employs instrumental calibrations that are specific to each filter rather than
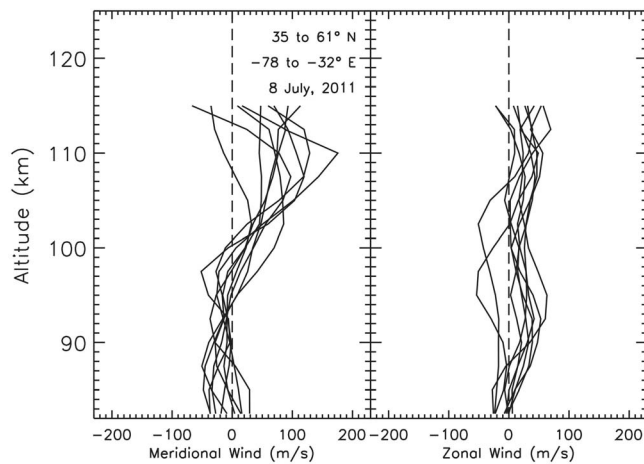
Figure 12. (left) Meridional and (right) zonal wind observations from TIDI during the time period immediately following launch of STS-135. Only wind profiles in the geographic region near the shuttle ascent ground track (Figure 1b) are shown. Uncertainties at 105 km altitude for either the meridional or zonal component are typically between 10 and 20 m/s and are included in Table 4.

one calibration for all and thereby corrects for wavelength-specific contributions.

[40] Figure 12 shows v11 TIDI meridional and zonal wind profiles for the time period immediately following STS-135 launch and for the geographic region between the launch location and the shuttle clouds observed near ALOMAR. The nine profiles shown are limited to the time period between 0.3 and 2.0 h after launch and have a vertical resolution between 2.5 and 5.0 km [*Killeen et al.*, 1999]. Tidal and planetary wave signatures have not been removed since this requires significant averaging of the data set over at least a month. Nonetheless, there is a persistent northward and eastward component to the winds in the lower thermosphere which agrees with the motion of the plume. In addition, the meridional wind speeds in this altitude region vary dramatically and can be remarkably large, with magnitudes up to 176 m/s at 110 km. The variability of these wind observations with altitude is moreover consistent with the observed large-scale shearing processes inferred directly from the plume observations discussed above. A quantitative analysis of the observed motion requires a parcel advection calculation over the indicated time period with a high vertical resolution model including detailed wind descriptions over the entire diurnal cycle so that mean winds, tides and planetary waves can be properly characterized. While such an analysis is beyond the scope of this paper, for completeness we show the TIDI wind observations at 105 km from Figure 12 in Table 4. Table 4 shows that the average wind speeds from these observations at the center of the shuttle plume are 71 ± 4 m/s northward and 15 ± 5 m/s eastward, which are generally consistent with the motion inferred from the satellite and ground-based observations presented herein.

[41] The CIPS satellite and RMR ground-based lidar data indicate that the brightest population of mesospheric clouds in the northern summer of 2011 equatorward of 71°N is strongly influenced by the STS-135 plume (Figures 8 and 10). This result is particularly compelling in the context of

the separate water vapor plume observations also presented, showing rapid transport toward the Arctic. Earlier work using the SBUV instrument indicated that shuttle main engine exhaust may produce brighter PMCs [*Stevens et al.*, 2005b], but the horizontal resolution of SBUV is 90 times lower than CIPS [*Benze et al.*, 2009], which prevented the identification of localized bursts such as those shown in Figure 7 near ALOMAR.

[42] In order to assess the impact of large amounts of lower thermospheric water vapor on the mesospheric cloud population we use the one-dimensional Community Aerosol and Radiation Model for Atmospheres (CARMA) as presented by *Rapp and Thomas* [2006]. For this preliminary estimate we choose a simple approach, wherein the model is run for the Rapp and Thomas reference case and then again with the plume water vapor added. We seek only to produce a qualitative estimate of the vertically integrated cloud brightness from water plumes, and not to reproduce details of the properties shown in Figures 11a and 11b, since the detailed vertical structure is controlled by small scale dynamics of which we do not have knowledge. Specifically we attempt to reproduce the observed variation of CIPS albedo and RMR integrated backscatter coefficient, which are less sensitive to the altitude profiles of the input properties. To indicate background conditions, Figure 13 shows the CARMA simulations of β_{int}, A and IWC using the same reference inputs as *Rapp and Thomas* [2006]. The results for this background case at the end of the 24-h simulation for IWC (also called ice column mass density) are consistent with those reported by Rapp and Thomas.

[43] As discussed by *Meier et al.* [2011], the plume is subject to both diffusion and photodissociation processes as it is transported from its point of injection. The diffusion processes can include both molecular and eddy diffusion. We ran the two-dimensional plume model for the same conditions as described by *Meier et al.* [2011] with only molecular diffusion and then with eddy diffusion added in order to assess how efficiently eddy diffusion can mix the water vapor down to the mesopause where ice can form.

[44] Figure 14a shows water vapor mixing ratios as a function of altitude and distance from the center of the plume injected at 106 km altitude after 16 h using only molecular diffusion. Here the water vapor does not reach the altitude of the cold summer mesopause (~88 km), so no ice forms and the results are the same as the reference case. Figure 14b shows results for the water vapor density from the same simulation.

[45] Figure 15a shows the same plume after 16 h but using an eddy diffusion coefficient of 400 m^2/s throughout the

Table 4. TIDI Wind Speeds at 105 km on 8 July 2011

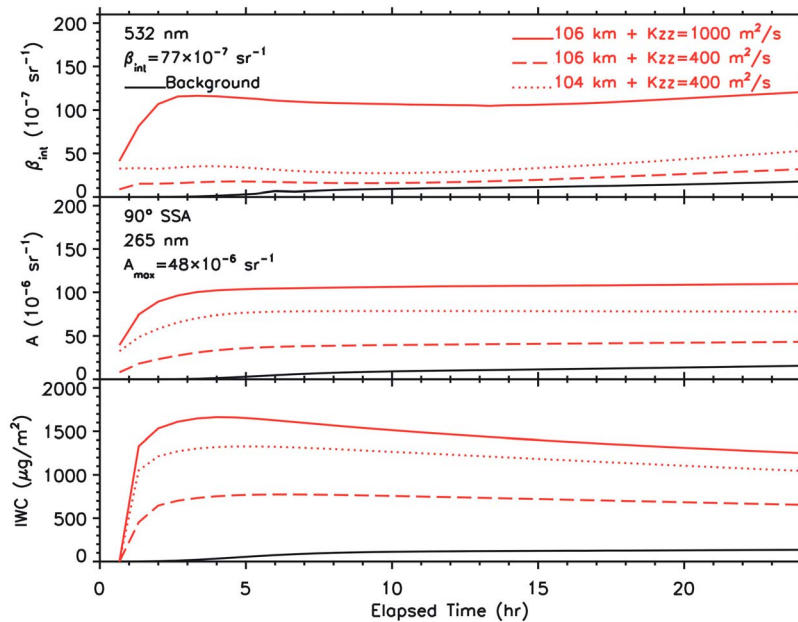| UT	LST	Lat	Lon	v (m/s)	u (m/s)
15:48	13:27	61	−34	54 ± 13	2 ± 14
15:50	13:32	54	−33	78 ± 13	35 ± 14
15:50	10:35	41	−78	56 ± 14	−31 ± 20
15:52	13:36	46	−33	104 ± 12	24 ± 14
15:52	10:58	35	−72	102 ± 15	16 ± 19
15:54	13:42	38	−32	48 ± 10	−7 ± 12
17:27	13:31	54	−58	84 ± 13	36 ± 14
17:29	13:36	46	−57	84 ± 12	17 ± 13
17:31	13:41	38	−56	26 ± 14	39 ± 15
Avg.: 16:24	12:58	46	−50	71 ± 4	15 ± 5

Figure 13. CARMA model simulations showing the integrated backscattered brightness (β_{int}) at 532 nm, the albedo (A) at 265 nm and the ice water content (IWC). The black curves represent the background case with inputs specified by *Rapp and Thomas* [2006]. The red curves are the results of the same simulation but with a lower thermospheric shuttle plume added and two different eddy diffusion coefficients used. The plume is simulated at two separate altitudes because of ambiguity in the initial altitude of injection (Figure 1a). The plume simulation is in good agreement with cloud observations following launch of STS-135, which indicate a peak β_{int} of 77×10^{-7} sr^{-1} and a peak A of 48×10^{-6} sr^{-1}.

plume region, a value that is generally consistent with previous observations in this region of the atmosphere [*Hocking*, 1990; *Lübken*, 1997; *Bishop et al.*, 2004; *Liu*, 2009]. We also show the water vapor density after the same amount of time in Figure 15b. For the case in which we have added eddy diffusion to the plume evolution, the water vapor is mixed down below 90 km to the mesopause where ice can form and it is this profile at the center of the plume (Distance = 0 km) that we use in our second simulation. Although the local mixing ratios indicated in Figure 15a are quite high, with a peak in excess of 10^4 ppmv near 115 km altitude, we note that (1) SMR and cWASPAM1 show strong evidence of transient high water vapor mixing ratios near ALOMAR during this time (Figures 4 and 6), and (2) once ice is formed then the high water vapor mixing ratios are depleted. In this simple simulation, we note that the model does not include any effects due to wind shears and it is assumed that the plume moves as a coherent parcel for 16 h. Thus strong eddy mixing provides a solution to the longstanding problem of how to move the plume water vapor down to the mesopause where temperatures are low enough to form PMCs.

[46] In addition to our background case and our case with $K_{zz} = 400$ m^2/s, we ran two more simulations that included eddy diffusion of the shuttle plume after 16 h of mixing and include results for each of these in Figure 13. These include an additional simulation using a higher eddy diffusion coefficient of 1000 m^2/s and also an initial plume altitude 2 km lower at 104 km using an eddy diffusion coefficient of 400 m^2/s. Given that we are using the climatologically averaged values of the background atmosphere, the agreement with the peak observed β_{int} (77 sr^{-1}) and A (48 sr^{-1}) is

very good. This is additional support for the formation of anomalously bright mesospheric clouds near 70°N on 9 July 2011 from STS-135.

[47] The large ice particles observed above 84 km and the inverted size profile shown in Figure 11a are also distinguishing features of the bright clouds observed on 9 July. A quantitative simulation of the detailed size profile is not possible without simultaneous measurements of temperature, water vapor and vertical winds as well as an accurate description of the concentration of meteoric smoke or some other nucleation site. None of these are available for the short time period studied herein and we are furthermore not privy to the age of the clouds, which would convey their stage of growth. Additional data on cloud characteristics given a concentrated water vapor source from above are needed to better constrain model results.

[48] The bright CIPS PMCs of 9 July shown in Figure 8 were observed over two consecutive orbits. The total ice mass reported by CIPS for these bright clouds is 15 t, which is a small fraction of the 350 t injected by the shuttle between 100 and 115 km. The potential contribution to the PMC population from other space traffic is listed in Table 3 and not considered in our estimates of ice mass. We therefore suggest that the shuttle and other space traffic are significant factors to formation of the brightest population of PMCs.

10. Summary

[49] The main engine plume of the final space shuttle launch and its effects were observed by a wide variety of
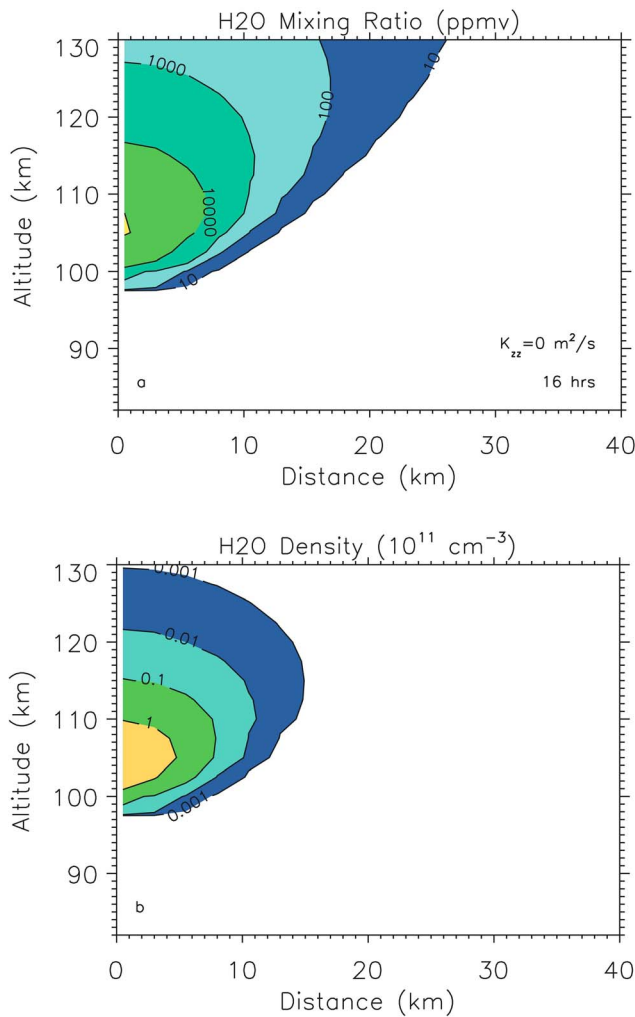
Figure 14. (a) Water vapor mixing ratios (in ppmv) of a two-dimensional plume simulation after 16 h of molecular diffusion for a plume injected at 106 km. (b) Water vapor densities (in 10^{11} cm^{-3}) for the same simulation.

satellite and ground-based instruments. These observations and our supporting model results have yielded new insights to global scale dynamics between 100 and 110 km as well as PMC formation from the shuttle plume. The primary conclusions are as follows.

[50] 1. Satellite water vapor observations show that the STS-135 water vapor plume spreads horizontally between about 3000 to 4000 km after only 18 h. This is the first quantitative determination of the horizontal extent of the shuttle's water vapor plume.

[51] 2. A portion of the STS-135 plume was transported from the east coast of the United States to the Arctic to form PMCs in 21 h.

[52] 3. Satellite and ground-based observations indicate that the integrated PMC brightness (or albedo) of the clouds following launch was a factor of 7 to 15 larger than the climatological average and brighter than at least 99% of all other PMCs.

[53] 4. Ground-based observations indicate that ice particle size (35 to 75 nm) and the altitude (82.8 km) of the STS-135 clouds are not significantly different from typical NLCs.

[54] 5. Ground-based observations also indicate that the particle size altitude profile of the STS-135 NLC is inverted such that smaller particles are at the bottom of the cloud and larger particles are at the top, with particle sizes of 70 nm above 84 km.

[55] 6. Our modeling shows that eddy diffusion can mix the plume water vapor down to the mesopause where ice can form if the eddy diffusion coefficient is between 400 to 1000 m^2/s.

[56] Further progress on this topic is limited by the available data and suggestions for future work include (1) lower thermospheric satellite observations of water vapor to monitor the contribution of space traffic to the global water vapor variability there (see Figure 4), (2) comprehensive observations of lower thermospheric winds and how they relate to global scale transport, and (3) analysis of the vertically integrated PMC brightness within the existing databases and comparison with space traffic activity and ambient lower thermospheric water vapor variability.

[57] Although there will not be another shuttle launch, space traffic worldwide continues virtually every week (e.g., Table 3) and the contribution of these smaller exhaust plumes
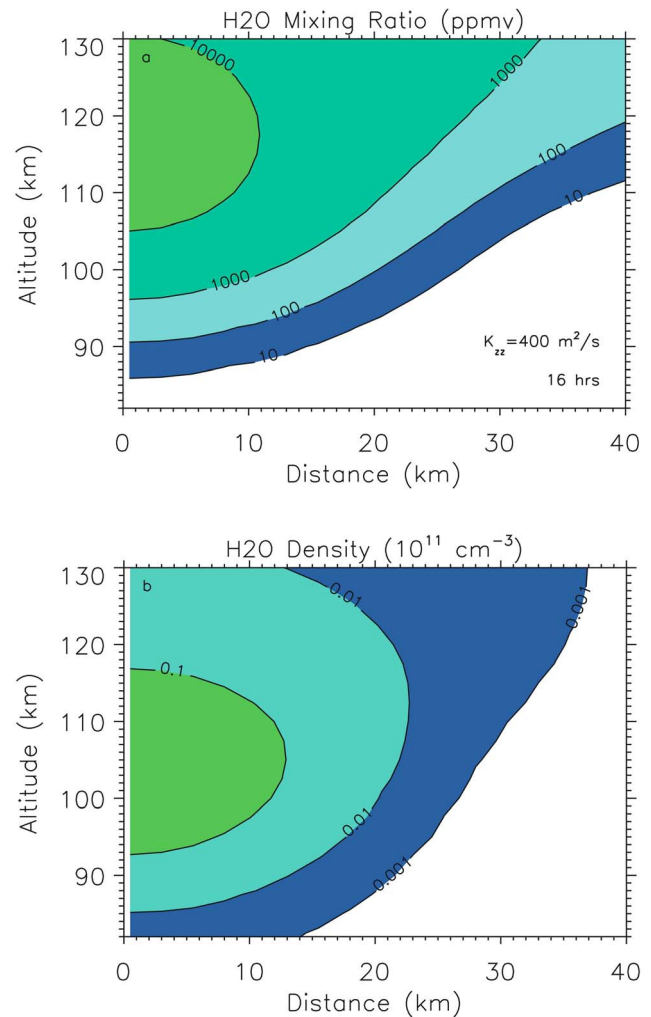

Figure 15. (a) Same as Figure 14a except using an eddy diffusion coefficient of 400 m^2/s. (b) Same as Figure 14b except using an eddy diffusion coefficient of 400 m^2/s.
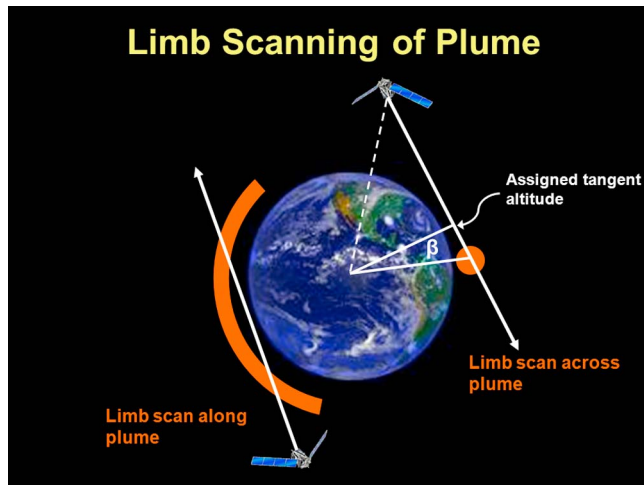
Figure A1. Sketch showing the limiting cases of limb scanning along the long dimension of a spherical shell plume (left) and across the transverse dimension of the shell (right). The plume can be located in the background (shown as $\beta > 0$) or in the foreground ($\beta < 0$) of the tangent point location. The LOS is indicated by the arrowed lines.

to the PMC record remains unquantified. The evidence of global-scale shearing processes in our data suggest that impacts on the PMC population may be determined more by how much effluent reaches the polar summer than by the size of the launch vehicle. Since water vapor is a common effluent of launch vehicle engines and the STS-135 exhaust represents only about 20% of all the liquid propellants used in launch vehicles during the 2011 PMC season, the evidence presented herein suggests that this source from above could form the brightest cloud population from one year to the next near 70°N. PMCs equatorward of this latitude are typically dimmer and could also be significantly affected by space traffic, including the latitudes near 60°N at which the clouds are most detectable to the naked eye.

Appendix A: Near and Far Field Effects on Plume Limb Viewing

[58] Analyses of SABER limb observations of water vapor plume radiances shown in Figure 2 and previous observations [*Siskind et al.*, 2003; *Meier et al.*, 2011] indicate that the observed heights are systematically lower than the typical injection height by about 7 ± 4 km. This discrepancy between expected and observed altitudes of the peak emission is significant. A likely explanation is that the apparent height assigned by the SABER algorithms to an observation is lower when the plume is not co-located with the SABER line-of-sight (LOS) tangent point location.

[59] To explore the effect of plume location on observed heights, we consider two limiting observing scenarios of radiances from a very simple plume model. The limiting cases apply to limb radiances only—not to higher level data products such as retrieved densities. The plume is assumed to have a very long cylindrical layer shape, at a fixed altitude (i.e., it follows Earth curvature). In order to isolate geometric effects, we assume that the curved cylinder is filled uniformly with water vapor. The first limiting case consists of a

scan across the plume, normal to the long dimension. The plume shape is a circle in this scan plane. This projection enables an assessment of the effect on the limb scan of locating the plume in the foreground or background relative to the tangent point. The second limiting case is a scan in a plane that includes the central axis of the plume. The projection in this plane is a spherical shell, which allows an assessment of plume dimension effects on the limb scan. The simplifying assumption of uniform density means that the column density and therefore the intensity will be proportional only to the path length through the object. The two geometries are shown in Figure A1. In all of the computations described below, the TIMED spacecraft is assumed to be at 630 km and the earth radius is 6371 km. Since the Odin orbital altitude is near 600 km, these results apply to the SMR water vapor observations of the shuttle plume as well.

A1. Scanning Normal to Plume Axis

[60] The limb scan geometry is depicted on the right side of Figure A1. We examine the sensitivity of the limb scan to the radius of the plume and its altitude (defined at the center of the circle), as well as its placement in the near field ($\beta < 0°$ in Figure A1) or far field ($\beta > 0°$) of the tangent point along the LOS. The tangent point is defined as the perpendicular intersection of the $\beta = 0°$ line and the LOS.

[61] Figure A2 shows limb scans for a plume of diameter 10 km centered at 106 km altitude. The left panel displays the intensity for near and far field angles, β ranging from $-3°$ (foreground) to $+3°$ (background). The foreground or near field case is plotted in red. The horizontal near and far field displacement distances along an arc of altitude 106 km are given by (6371 km + 106 km) $\times$ β (radian), so $\beta = 3°$ corresponds to about 340 km away from the 106 km tangent point.

[62] When the plume is exactly located at the $\beta = 0°$ point, the observation tangent altitude equals the plume altitude. As the plume moves into the far field, its apparent altitude (given by peak intensity) decreases, but not quite as rapidly as in the near field. This is due to the decreasing apparent size of the plume cross section as it moves away from the spacecraft. The right panel shows the altitude of peak intensity versus β. As the plume diameter increases, the width of the plume radiance profile increases (not shown), as expected, but the altitude change with β does not. For a plume at 112 km the widths of the intensity profile are essentially the same as the 106 km case. The location in the near field or far field by only 300 km from the line-of-sight tangent point can produce apparent altitude decreases of order 7 km, consistent with the SABER observations.

A2. Scanning Along the Plume Axis

[63] This second limiting case is illustrated on the left side of Figure A1. We varied the height and width of the shell to determine their effects on the apparent observation altitude. Figure A3 shows how the shell width influences the limb scan for a plume altitude of 106 km (center of the shell). The left panel shows the relative intensity versus tangent altitude for plume diameters of 2, 6, 10 and 14 km. The horizontal dashed lines indicate the true altitude of the plume (shell center). Intensities have been normalized so that the vertical column density through the uniform shell is the same in each
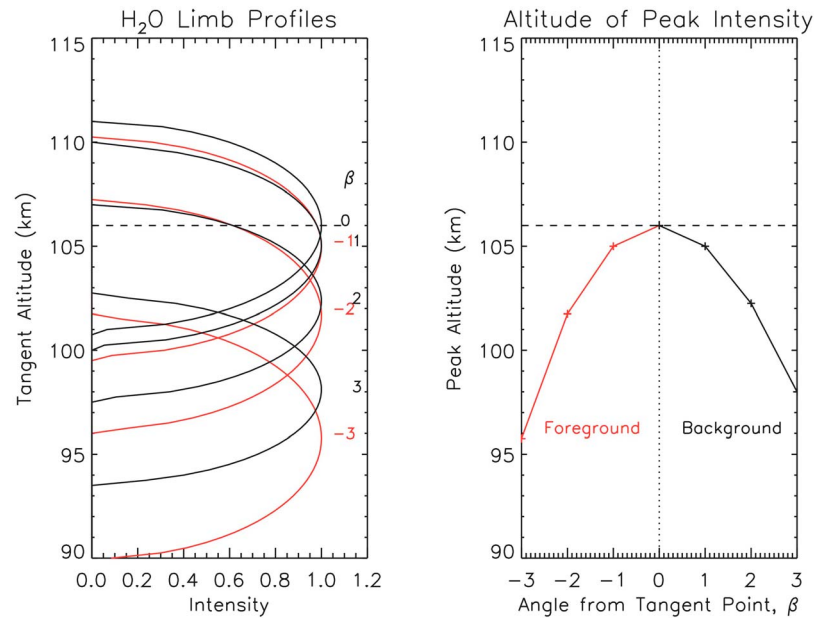
Figure A2.   (left) Limb scans along the transverse dimension of a circular plume of diameter 10 km, located at 106 km altitude. Scans are for the labeled values of β, as defined in Figure A1. (right) Peak altitude versus angle from the tangent point of the plume.

case. This does not affect the altitude dependence. As the plume width increases, the altitude of peak brightness drops due to the changed path length, even though the true altitude of the center of the plume remains at 106 km. This is a consequence of the fact that the maximum path through the shell is located where the tangent altitude is just at the bottom boundary of the shell. For a wider shell, that tangent point is lower. The observed width of the shell increases with increasing width, as expected.

[64]   The right panel of Figure A3 shows how the altitude of peak brightness decreases with increasing shell width. Thus as a real plume expands with time, its apparent height is expected to decrease. For a plume vertical width of 14 km, the drop in peak altitude is about 7 km. Virtually identical behavior in peak altitude change and limb intensity shape is found for a plume at 112 km [*Meier et al.*, 2011]; the only difference is that the peak altitudes are shifted upward by 6 km from the 106 km plume. This behavior is close to the
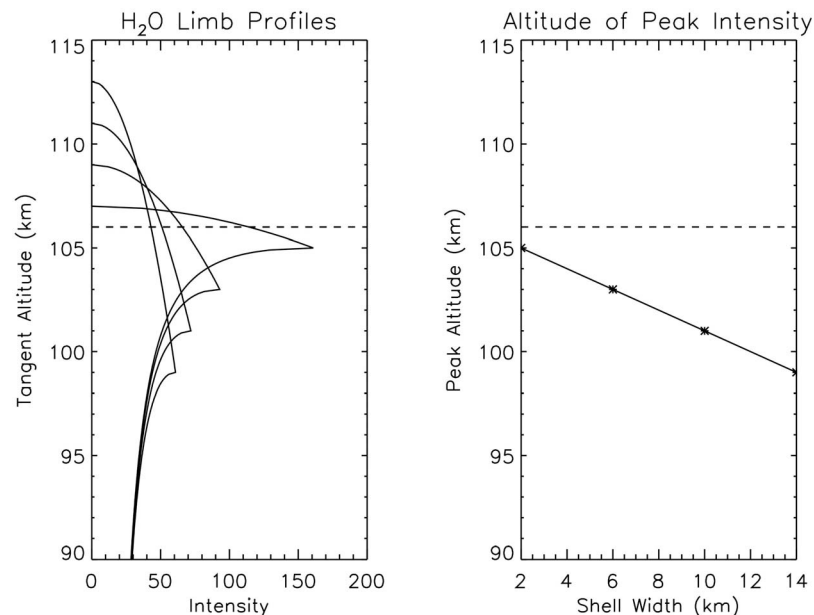

Figure A3.   (left) Limb scans of the long dimension of a spherical shell plume with thicknesses of 2, 6, 10 and 14 km. The 14 km case is the widest profile. The center of the shell is at 106 km. (right) Altitude of peak intensity versus width of the shell.

discrepancy between the injection altitude (106 km) and the altitudes observed by SABER, and consistent with the decrease in observed altitude with elapsed time.

A3. Summary

[65] The tangent point is by definition the lowest location along the LOS. Thus any plume located along that line will be at a higher altitude than reported in the instrument attitude information. For limb scans through the transverse (narrow) dimension of a plume by SABER or SMR, the altitude of peak intensity decreases with increasing or decreasing distance of the plume from the tangent point along the LOS, even though the true altitude is not changed. For limb scans through the long dimension, the apparent altitude decreases with increasing plume width. These two limiting cases offer plausible geometrical explanations of why limb observations of plumes consistently measure (apparent) altitudes lower than the true altitude by about 7 km.

References

American Institute of Aeronautics and Astronautics (AIAA) (1991), *Atmospheric Effects of Chemical Rocket Propulsion*, 52 pp., New York.

Bailey, S. M., et al. (2009), Phase function of polar mesospheric cloud ice as observed by the CIPS instrument on the AIM satellite, *J. Atmos. Sol. Terr. Phys.*, *71*, 373–380, doi:10.1016/j.jastp.2008.09.039.

Baumgarten, G., and J. Fiedler (2008), Vertical structure of particle properties and water content in noctilucent clouds, *Geophys. Res. Lett.*, *35*, L10811, doi:10.1029/2007GL033084.

Baumgarten, G., J. Fiedler, and M. Rapp (2010), On microphysical processes of noctilucent clouds (NLC): Observations and modeling of mean and width of the particle size-distribution, *Atmos. Chem. Phys.*, *10*, 6661–6668, doi:10.5194/acp-10-6661-2010.

Baumgarten, G., et al. (2012), On the horizontal and temporal structure of noctilucent clouds as observed by satellite and lidar at ALOMAR (69N), *Geophys. Res. Lett.*, *39*, L01803, doi:10.1029/2011GL049935.

Benze, S., et al. (2009), Comparison of polar mesospheric cloud measurements from the Cloud Imaging and Particle Size experiment and the solar backscatter ultraviolet instrument in 2007, *J. Atmos. Sol. Terr. Phys.*, *71*, 365–372, doi:10.1016/j.jastp.2008.07.014.

Bishop, J. (1999), Transport of resonant atomic hydrogen emissions in the thermosphere and geocorona: Model description and applications, *J. Quant. Spectrosc. Radiat. Transf.*, *61*, 473–491, doi:10.1016/S0022-4073(98)00031-4.

Bishop, R. L., M. F. Larsen, J. H. Hecht, A. Z. Liu, and C. S. Gardner (2004), TOMEX: Mesospheric and lower thermospheric diffusivities and instability layers, *J. Geophys. Res.*, *109*, D02S03, doi:10.1029/2002JD003079.

Collins, R. L., et al. (2009), Noctilucent cloud in the western Arctic in 2005: Simultaneous lidar and camera observations and analysis, *J. Atmos. Sol. Terr. Phys.*, *71*, 446–452, doi:10.1016/j.jastp.2008.09.044.

DeLand, M. T., E. P. Shettle, G. E. Thomas, and J. J. Olivero (2007), Latitude-dependent long-term variations in polar mesospheric clouds from SBUV version 3 PMC data, *J. Geophys. Res.*, *112*, D10315, doi:10.1029/2006JD007857.

Fiedler, J., et al. (2011), NLC and the background atmosphere above ALOMAR, *Atmos. Chem. Phys.*, *11*, 5701–5717, doi:10.5194/acp-11-5701-2011.

Frisk, U., et al. (2003), The Odin satellite: I. Radiometer design and test, *Astron. Astrophys.*, *402*, L27–L34, doi:10.1051/0004-6361:20030335.

Hallgren, K., and P. Hartogh (2012), First detection of tidal behaviour in polar mesospheric water vapour by ground based microwave spectroscopy, *Atmos. Chem. Phys.*, *12*, 3753–3759, doi:10.5194/acp-12-3753-2012.

Hartogh, P., G. R. Sonnemann, M. Grygalashvyly, U. Berger, and F.-J. Lübken (2010), Water vapor measurements at ALOMAR over a solar cycle compared with model calculations by LIMA, *J. Geophys. Res.*, *115*, D00I17, doi:10.1029/2009JD012364.

Hocking, W. K. (1990), Turbulence in the region 80–120 km, *Adv. Space Res.*, *10*(12), 153–161, doi:10.1016/0273-1177(90)90394-F.

Isakowitz, S. J., J. P. Hopkins Jr., and J. B. Hopkins (1999), *International Reference Guide to Space Launch Systems*, 3rd ed., Am. Inst. of Aeronaut. and Astronaut., Reston, Va.

Kelley, M. C., C. E. Seyler, and M. F. Larsen (2009), Two-dimensional turbulence, space shuttle plume transport in the thermosphere, and a possible relation to the Great Siberian Impact Event, *Geophys. Res. Lett.*, *36*, L14103, doi:10.1029/2009GL038362.

Kelley, M. C., M. J. Nicolls, R. H. Varney, R. L. Collins, R. Doe, J. M. C. Plane, J. Thayer, M. Taylor, B. Thurairajah, and K. Mizutani (2010), Radar, lidar, and optical observations in the polar summer mesosphere shortly after a space shuttle launch, *J. Geophys. Res.*, *115*, A05304, doi:10.1029/2009JA014938.

Kellogg, W. W. (1964), Pollution of the upper atmosphere by rockets, *Space Sci. Rev.*, *3*, 275–316, doi:10.1007/BF00180267.

Killeen, T. L., et al. (1999), TIMED Doppler Interferometer (TIDI), *Proc. SPIE*, *3756*, 289–301, doi:10.1117/12.366383.

Liu, A. Z. (2009), Estimate eddy diffusion coefficients from gravity wave vertical momentum and heat fluxes, *Geophys. Res. Lett.*, *36*, L08806, doi:10.1029/2009GL037495.

Liu, H.-L. (2007), On the large wind shear and fast meridional transport above the mesopause, *Geophys. Res. Lett.*, *34*, L08815, doi:10.1029/2006GL028789.

Lossow, S., J. Urban, P. Eriksson, D. Murtagh, and J. Gumbel (2007), Critical parameters for the retrieval of mesospheric water vapour and temperature from Odin/SMR limb measurements at 557 GHz, *Adv. Space Res.*, *40*, 835–845, doi:10.1016/j.asr.2007.05.026.

Lossow, S., et al. (2009), Wintertime water vapor in the polar upper mesosphere and lower thermosphere: First satellite observations by Odin submillimeter radiometer, *J. Geophys. Res.*, *114*, D10304, doi:10.1029/2008JD011462.

Lübken, F.-J. (1997), Seasonal variation of turbulent energy dissipation rates at high latitudes as determined by in situ measurements of neutral density fluctuations, *J. Geophys. Res.*, *102*, 13,441–13,456, doi:10.1029/97JD00853.

McClintock, W. E., et al. (2009), The cloud imaging and particle size experiment on the Aeronomy of Ice in the mesosphere mission: Instrument concept, design, calibration, and on-orbit performance, *J. Atmos. Sol. Terr. Phys.*, *71*, 340–355, doi:10.1016/j.jastp.2008.10.011.

Meier, R. R., J. M. C. Plane, M. H. Stevens, L. J. Paxton, A. B. Christensen, and G. Crowley (2010), Can molecular diffusion explain Space Shuttle plume spreading?, *Geophys. Res. Lett.*, *37*, L08101, doi:10.1029/2010GL042868.

Meier, R. R., M. H. Stevens, J. M. C. Plane, J. T. Emmert, G. Crowley, I. Azeem, L. J. Paxton, and A. B. Christensen (2011), A study of space shuttle plumes in the lower thermosphere, *J. Geophys. Res.*, *116*, A12322, doi:10.1029/2011JA016987.

Niciejewski, R., Q. Wu, W. Skinner, D. Gell, M. Cooper, A. Marshall, T. Killeen, S. Solomon, and D. Ortland (2006), TIMED Doppler Interferometer on the Thermosphere Ionosphere Mesosphere Energetics and Dynamics satellite: Data product overview, *J. Geophys. Res.*, *111*, A11S90, doi:10.1029/2005JA011513.

Niciejewski, R., W. Skinner, M. Cooper, A. Marshall, R. R. Meier, M. H. Stevens, D. Ortland, and Q. Wu (2011), Verification of large-scale rapid transport in the lower thermosphere: Tracking the exhaust plume of STS-107 from launch to the Antarctic, *J. Geophys. Res.*, *116*, A05302, doi:10.1029/2010JA016277.

Pumphrey, H. C., A. Lambert, and N. J. Livesey (2011), Observation of the exhaust plume from the space shuttle main engines using the microwave limb sounder, *Atmos. Meas. Tech.*, *4*, 89–95, doi:10.5194/amt-4-89-2011.

Rairden, R. L., L. A. Frank, and J. D. Crain (1986), Geocoronal imaging with Dynamics Explorer, *J. Geophys. Res.*, *91*, 13,613–13,630, doi:10.1029/JA091iA12p13613.

Rapp, M., and G. E. Thomas (2006), Modeling the microphysics of mesospheric ice particles: Assessment of current capabilities and basic sensitivities, *J. Atmos. Sol. Terr. Phys.*, *68*, 715–744, doi:10.1016/j.jastp.2005.10.015.

Russell, J. M., III, et al. (2009), The Aeronomy of Ice in the Mesosphere (AIM) mission: Overview and early science results, *J. Atmos. Sol. Terr. Phys.*, *71*, 289–299, doi:10.1016/j.jastp.2008.08.011.

Shettle, E. P., M. T. DeLand, G. E. Thomas, and J. J. Olivero (2009), Long term variations in the frequency of polar mesospheric clouds in the Northern Hemisphere from SBUV, *Geophys. Res. Lett.*, *36*, L02803, doi:10.1029/2008GL036048.

Siskind, D. E., M. H. Stevens, J. T. Emmert, D. P. Drob, A. J. Kochenash, J. M. Russell III, L. L. Gordley, and M. G. Mlynczak (2003), Signatures of shuttle and rocket exhaust plumes in TIMED/SABER radiance data, *Geophys. Res. Lett.*, *30*(15), 1819, doi:10.1029/2003GL017627.

Stevens, M. H., C. R. Englert, and J. Gumbel (2002), OH observations of space shuttle exhaust, *Geophys. Res. Lett.*, *29*(10), 1378, doi:10.1029/2002GL015079.

Stevens, M. H., J. Gumbel, C. R. Englert, K. U. Grossmann, M. Rapp, and P. Hartogh (2003), Polar mesospheric clouds formed from space shuttle exhaust, *Geophys. Res. Lett.*, *30*(10), 1546, doi:10.1029/2003GL017249.

Stevens, M. H., R. R. Meier, X. Chu, M. T. DeLand, and J. M. C. Plane (2005a), Antarctic mesospheric clouds formed from space shuttle exhaust, *Geophys. Res. Lett.*, *32*, L13810, doi:10.1029/2005GL023054.

Stevens, M. H., C. R. Englert, M. T. DeLand, and M. Hervig (2005b), The polar mesospheric cloud mass in the Arctic summer, *J. Geophys. Res.*, *110*, A02306, doi:10.1029/2004JA010566.

Thomas, G. E. (1996), Is the polar mesosphere the miner's canary of global change?, *Adv. Space Res.*, *18*(3), 149–158, doi:10.1016/0273-1177(95)00855-9.

Urban, J., et al. (2007), Global observations of middle atmospheric water vapour by the Odin satellite: An overview, *Planet. Space Sci.*, *55*, 1093–1102, doi:10.1016/j.pss.2006.11.021.

Yue, J., and H.-L. Liu (2010), Fast meridional transport in the lower thermosphere by planetary-scale waves, *J. Atmos. Sol. Terr. Phys.*, *72*, 1372–1378, doi:10.1016/j.jastp.2010.10.001.

Zhang, S. P., C. McLandress, and G. G. Shepherd (2007), Satellite observations of mean winds and tides in the lower thermosphere: 2. Wind Imaging Interferometer monthly winds for 1992 and 1993, *J. Geophys. Res.*, *112*, D21105, doi:10.1029/2007JD008457.